Diagnosing the Initiation of an Extreme North Pacific Jet Retraction using Piecewise Tendency Diagnosis

by

MELISSA BREEDEN and JONATHAN E. MARTIN

Department of Atmospheric and Oceanic Sciences
University of Wisconsin-Madison
1225 W. Dayton St.
Madison, WI 53706
608-262-9845
jemarti1@wisc.edu

Key Words: jet stream variability, midlatitude weather systems, blocking, geophysical fluid dynamics

ABSTRACT

An unusually prolonged retraction of the tropopause-level jet transformed the circulation in the north Pacific for weeks in mid-February and March 2006 and preceded the development of a long-lived negative Pacific-North American Pattern. The initiation of this jet retraction, associated with a series of anticyclonic/LC1 wave breaking events at high latitude, is investigated through the lens of quasi-geostrophic piecewise tendency analysis. Two key anticyclonic anomalies divert and retract the jet through serial LC1 wave breaking events, mostly confined to the 315-330K isentropic layer and occurring in regions of strong deformation. The rapid development of the first anomaly coincided with the beginning of retraction, and its development is diagnosed in a QG framework in order to quantify contributions to QG height tendencies from various processes. The resultant analysis reveals that growth was induced by a deep PV intrusion that perturbed the jet, while the remainder of the ridge's lifecycle was largely governed by upper-level deformation in the jet exit region. Deformation facilitated both growth and decay, as the phasing between the ridge and deformation changed. Baroclinic development also contributed to growth, but substantially less than observed by previous studies.

1. Introduction

The tropopause-level jet stream in the north Pacific is one of the most dynamically influential features on the planet, affecting both the day-to-day sensible weather as well as elements of the low-frequency general circulation around the globe (Palmén and Newton 1948; Namias and Clapp 1949). The jet stream varies in strength and position throughout the year, becoming stronger in winter when the Northern Hemisphere meridional temperature gradient intensifies (Palmén 1948; Fleming et al. 1987; Weickmann and Chervin 1988; Newman and Sardeshmukh 1998). In addition to a pronounced seasonal cycle, substantial intra-seasonal variability prevails, often associated with high-impact weather including atmospheric blocking and changes in the track and frequency of extratropical cyclones (Rex 1953; Palmén and Newton 1969; Dole and Gordon 1983).

Motivated by the changes in the position and strength of the jet on monthly, weekly, and daily timescales, many studies have investigated coherent modes of variability in the middle-to-upper troposphere that impact the jet. Wallace and Gutzler (1981) investigated the covariance of monthly-mean 500hPa geopotential height anomalies for December-February 1962-1977, by correlating various base points around the Northern Hemisphere with the total two-dimensional height field. Their analysis revealed the presence of large-scale 'teleconnection' patterns where certain geopotential height anomalies separated by great distances varied together, often as dipoles or quadrupoles. In the Pacific basin, the Pacific-North American (PNA) pattern, a quadrupole structure, whose positive phase is characterized by an anticyclonic anomaly in the subtropical central Pacific, a sprawling cyclonic feature to its north in the midlatitudes, followed by another trough-ridge pair downstream over the west coast of North America and the southeastern United States, prevailed.

Another curious characteristic of the jet is that it can both modulate, and be modulated by, the lifecycle of baroclinic eddies. Simmons and Hoskins (1980) used a baroclinic channel model and varied the shear in the domain to investigate how this alteration to the background state affects the lifecycle of a prescribed, small-amplitude perturbation. Thorncroft et al. (1993) performed a similar experiment at higher resolution, and found that enhancing the cyclonic shear in the domain leads to what they termed an 'LC2' type lifecycle, wherein a developing cyclone remains on the cyclonic shear side of the jet and continues to rotate cylonically as it decays. In contrast, the same initial disturbance growing in a basic state characterized by relatively reduced cyclonic shear was observed to migrate from the cyclonic to anticyclonic shear side of the jet, while changing tilt from NW/SE (negative tilt) to NE/SW (positive tilt). In the latter example, a streamer of high, cyclonic potential vorticity (PV) air is cutoff while the disturbance decays, reflective of Rossby wave breaking, defined as the reversal of the climatological meridional PV gradient which points south-north (McIntyre and Palmer 1983). Thorncroft et al. (1993) dubbed this particular lifecycle 'LC1', terminology that has been adopted by many authors since.

Teleconnections, jet variability and wave breaking are physically related, and clarifying the finer points of their relationships is an active area of research. Martius et al. (2007) showed how the frequency of LC1/LC2 wave breaking events, identified via PV streamers on various isentropic surfaces, differed significantly during various phases of well-known teleconnection patterns like the PNA and North Atlantic Oscillation (NAO). Pertinent to the present study is the reduction in LC2 (cyclonic) wave breaking associated with the negative polarity of the PNA, during which time a sprawling anticyclone is present in the central north Pacific and the jet is retracted. Martius et al. (2007) found the primary change in wave breaking frequency on 310K during the negative PNA occurs in the vicinity of the midlatitude anticyclone, which suppresses

baroclinic wave activity and cyclone development in that region. Subtropical (or Kona) cyclogenesis, known to enhance Hawaiian precipitation (Otkin and Martin 2004), is more frequent during this PNA phase due to the diverted waveguide. Franzke et al. (2011) examined the synoptic evolution of each phase of the PNA and found that the negative phase coincides with a weaker jet and a series of anticyclonic wave breaking events, consistent with the results of Martius et al (2007).

The central Pacific anomalies associated with the PNA are similar to the dipole in the leading mode of upper level (250-300mb) zonal wind speed in the North Pacific region, previously identified using empirical orthogonal function (EOF) analysis (Eichelberger and Hartmann 2007; Athanasiadis et al. 2009). This mode of variability represents the zonal extending or retracting of the jet exit region (EOF1), while the second mode indicates a north/south shifting of the exit region (EOF2, Athanasiadis et al., 2009; Jaffe et al., 2011; Griffin and Martin 2017). Otkin and Martin (2004) found that the frequency of subtropical cyclones in the basin is greatly modulated by the zonal extent of the upper level jet, captured by EOF1. In particular, a retracted jet is associated with more frequent subtropical 'Kona Low' systems, consistent with the results of Martius et al. (2007). The results from Otkin and Martin (2004) prompted an interest in the evolution of jet retractions in particular, given their association with Hawaiian precipitation.

Jaffe et al. (2011; hereafter JM) first defined criteria for a jet retraction using two independent methods, and examined the composite evolution of the three-dimensional flow field before, during and after retraction onset (Fig.1). Retractions are objectively identified when the mean wind speed in a latitude-longitude box in the central Pacific is less than 10 ms^{-1} below climatology for at least five consecutive days (box location: 25°-40°N, 180°-200°E; JM Fig.2).

94 This location coincides with the greatest amplitude in the pattern of EOF1 of 300mb zonal wind
95 (JM Fig.4). Each case was then visually inspected to verify that the objective identification
96 scheme was truly selecting a retraction, and not a north/south shift in a continuous jet core as
97 represented by EOF2. A total of 19 cases were confirmed by both methods from November-
98 March, 1980-2007.
99 Ten days before retraction onset (Fig.1a), no distinct upper level features are observed,
100 while the jet extends past Hawaii. Five days prior, the jet is still extended, now accompanied by a
101 cyclone in the left exit region and a high-amplitude ridge located downstream over western
102 North America. An equivalent barotropic, sprawling anticyclone in the midlatitude central
103 Pacific follows retraction, accompanied by a linear, cyclonic anomaly to its south in the
104 subtropics (Fig.1c-e). Together the circulation of these two features is ideally located to create
105 anomalous easterly winds that counter the westerly jet and maintain a retracted state.
106 Additionally, by Day +5 (Fig.1d), anomalies similar to the negative PNA pattern are exceedingly
107 clear. How the anomaly pattern reverses between Day -5 and Day 0 is not clear from composite
108 analysis, even looking at the daily evolution. Therefore, the present case study seeks to reveal
109 additional information regarding the dynamics that *initiate* the development of the evolution that
110 leads to such dramatic jet transitions.
111 This study examines the initiation of an extreme retraction that occurred from February-
112 March 2006, and led to an unprecedented period of rainfall, flooding and mudslides in Hawaii
113 (Jayawardena and Chen (2010); Climate Prediction Center). Of particular interest are the links
114 between jet variability, wave breaking, and the PNA. The first paper will provide a synoptic
115 overview of the 2006 case and investigate the lifecycle of a high-amplitude ridge that facilitates
116 retraction. The second paper will explicitly examine the role of features identified in the

synoptic overview, and how they contributed to jet retraction. In this paper, Section 2 will outline the data and methodology employed in the analysis, and Section 3 will provide a synoptic overview of the case. Piecewise tendency diagnosis, first introduced by Nielsen-Gammon and Lefèvre (1996), will then be applied to understand the lifecycle of a key feature related to retraction in Section 4. Discussion and conclusions will follow in Section 5.

2. Data and Methodology

a. Data

The ensuing analysis employs European Centre for Medium-Range Weather Forecasting (ECMWF) ERA-interim gridded data, accessed at 1°x1° spatial resolution and six hourly temporal resolution, via the online archive (Berrisford et al., 2011). The ERA-Interim data set optimally combines observations (including those from polar orbiting and geostationary satellites) using a four-dimensional variational analysis (4D-Var) scheme, with model output, to create a Reanalysis dataset from 1979 to present. Geopotential was accessed on pressure levels from 1000-50hPa at intervals of 50hPa. The dynamic tropopause was considered in terms of Ertel (1940) potential vorticity on the 2PVU surface (1PVU = 10^{-6}K kg^{-1}m^{2}s^{-1}). Potential temperature (θ) on 2PVU is output by ECMWF, found by searching below 98hPa for the 2PVU value, and then evaluating θ at that location (Berrisford et al., 2011). If the 2PVU value is not located below 98hPa, no value of θ is included.

The first empirical orthogonal function (EOF) of 250mb zonal wind was computed using National Center for Atmospheric Research (NCAR)/NCEP Reanalysis 2 output at 1°x1° spatial resolution and six-hourly temporal resolution for November-March 1980-2010 (*provided by the NOAA/OAR/ESRL PSD*). The corresponding principal component time series (PC1) was averaged to a daily mean, and the EOFs were computed after the 30-year daily climatology was

140 removed. The daily-mean Pacific-North American pattern index was accessed from the Climate
141 Prediction Center (CPC) online archive and was calculated using Rotated Principal Component
142 Analysis introduced by Barnston and Livesey (1987). NCEP/NCAR Reanalysis I data was used
143 in the CPC analysis, performed over the period 1950-2014.

144 *b. Anomaly Calculations*

145 Standardized height anomalies were computed using ERA-Interim output, by calculating
146 the 1979-2016 average for each six-hour time step. This climatology is then subtracted from the
147 total height field, and the resulting anomalies are standardized. Potential temperature anomalies
148 on 2PVU were calculated in the same manner, and then the four six-hourly anomalies for each
149 day were averaged to produce a daily anomaly. The potential temperature anomalies were not
150 standardized.

151 *c. Piecewise Tendency Diagnosis*

152 The quasi-geostrophic (QG) system can be used to arrive at a useful relationship between
153 quasigeostrophic potential vorticity (QGPV) and geopotential. QGPV is the sum of the
154 geostrophic relative vorticity, a stability term, and planetary vorticity (1). The sum reduces to the
155 three-dimensional Laplacian of geopotential ($\mathcal{L}(\phi)$) and planetary vorticity (1). Here,
156 $\nabla^2 = (\frac{\partial^2}{\partial x^2}, \frac{\partial^2}{\partial y^2})$, the two-dimensional Laplacian, ϕ represents deviations from the reference
157 atmosphere geopotential, f is the coriolis parameter, and σ is the reference atmosphere static
158 stability ($\sigma = -\frac{\alpha}{\theta}\frac{d\theta}{dp}$), where α is specific volume.

159 $$q = f + \frac{1}{f_o}\nabla^2\phi + f_o\frac{\partial}{\partial p}\left(\frac{1}{\sigma}\frac{\partial \phi}{\partial p}\right) = f + \mathcal{L}(\phi) \qquad (1)$$

160 Holopainen and Karola (1991) and Hakim et al. (1996) demonstrated the utility of
161 linearizing the total QGPV field about a basic state and then inverting the full-column

perturbation QGPV, q'_{tot}, to retrieve the balanced geopotential height field (2a). As $\mathcal{L}$ is a linear operator, q'_{tot} can be split into components that linearly combine to the sum, without any loss of information. Here q'_{tot} is split into two pieces, one from an upper layer extending from 50-500hPa, (q'_u), and one from a lower layer stretching from 550-1000hPa, (q'_l) (2b). The circulation associated with each piece of the perturbation QGPV extends throughout the troposphere and is distinguishable using this technique.

$$\phi'_{tot} = \mathcal{L}^{-1}(q'_{tot}) \quad (2a)$$

$$\phi'_{tot} = \phi'_u + \phi'_l = \mathcal{L}^{-1}(q'_u) + \mathcal{L}^{-1}(q'_l) \quad (2b)$$

Additionally, surface potential temperature at the lower boundary is incorporated after Bretherton (1966), who demonstrated that a positive (negative) θ anomaly at the surface can be represented as a positive (negative) QGPV anomaly. Here surface θ effects are incorporated through a Neumann boundary condition (3a) as in Nielsen-Gammon and Lefèvre (1996)[1].

$$\frac{\partial \phi}{\partial p} = -\frac{R}{p}\left(\frac{p}{p_o}\right)^{\kappa} \theta \quad (3a)$$

Hakim et al. (1996) introduced a prognostic piecewise QGPV inversion wherein geostrophic QGPV advection is inverted to attain QG height tendencies. Nielsen-Gammon and Lefèvre (1996, hereafter NGL) further partitioned the advection term to quantify the contributions made by specific processes to the total QG height tendencies. They demonstrated

[1] One further modification is made to retain the consistency between each *q'* field (upper/lower) and the surface θ field used in the inversion. Previous studies balance the surface θ field with only q'_l but there is also a piece of surface θ that is associated with q'_u (a smaller but nonnegligible contribution). In the present case the two surface θ fields are separated, and each QGPV piece is inverted with its corresponding θ field at the lower boundary. The surface θ fields are distinguished by first inverting q'_l with a Dirichlet lower boundary condition, in which the observed geopotential height anomaly is prescribed in the solution. The difference in surface θ calculated using the resultant height field and (3a), and that attained by inverting the *unpartitioned* q'_{tot} field is attributed to q'_u, and has a magnitude of +/- 5K (~25% of the observed 1000mb temperature anomalies).

179 the utility of this method, Piecewise Tendency Diagnosis (PTD), through a rigorous investigation
180 of the development of a mobile trough over the United States.

181 The mathematical steps taken to arrive at an expression for piecewise QG height
182 tendencies are repeated here. First, the Eulerian time tendency of QGPV reduces to the 3D
183 Laplacian of height tendencies (4), so that inverting the local QGPV tendency field yields QG
184 height tendencies (5). Assuming adiabatic and frictionless flow, QGPV is conserved following
185 the geostrophic flow, and geostrophic QGPV advection can be substituted for the local time
186 tendency $\frac{\partial q}{\partial t}$ (right hand side of (5)). The advection expression can be further separated into
187 several terms that represent distinct physical processes by linearizing the advection around a
188 time-mean basic state (denoted by overbars), and partitioning the anomalous QGPV and wind
189 fields into upper (q'_u, $\boldsymbol{v}'_{gu}$) and lower (q'_l, $\boldsymbol{v}'_{gl}$) layers as previously described. The anomalous
190 geostrophic wind fields associated with the upper and lower layers, $\boldsymbol{v}'_{gu}$ and $\boldsymbol{v}'_{gl}$, are calculated
191 using the geopotential fields attained from inverting q'_u and q'_l, including their respective surface
192 temperature anomalies (7a, 7b).

193 $$\frac{\partial q}{\partial t} = \frac{1}{f_o}\nabla^2\left(\frac{\partial \phi}{\partial t}\right) + f_o\frac{\partial}{\partial p}\left(\frac{1}{\sigma}\frac{\partial}{\partial p}\left(\frac{\partial \phi}{\partial t}\right)\right) = \mathcal{L}\left(\frac{\partial \phi}{\partial t}\right) \quad (4)$$

194 $$\frac{\partial \phi}{\partial t} = \mathcal{L}^{-1}\left(\frac{\partial q}{\partial t}\right) = \mathcal{L}^{-1}(-\boldsymbol{v}_g \cdot \nabla q) \quad (5)$$

195

196 A B C

197 $$\frac{\partial \phi'_u}{\partial t} = \mathcal{L}^{-1}\left(-\overline{\boldsymbol{v}}_g \cdot \nabla q'_u\right) + \mathcal{L}^{-1}\left(-\boldsymbol{v}'_{gu} \cdot \nabla \overline{q}_u\right) + \mathcal{L}^{-1}\left(-\boldsymbol{v}'_{gl} \cdot \nabla \overline{q}_u\right) \quad (6)$$

198

199

200 D E

201 $$+\mathcal{L}^{-1}\left(-\boldsymbol{v}'_{gu} \cdot \nabla q'_u\right) + \mathcal{L}^{-1}\left(-\boldsymbol{v}'_{gl} \cdot \nabla q'_u\right)$$

202
203
204 $$\boldsymbol{v}'_{gu} = \frac{1}{f_o}\boldsymbol{k} \times \nabla(\mathcal{L}^{-1}(q_u{}')) \qquad \boldsymbol{v}'_{gl} = \frac{1}{f_o}\boldsymbol{k} \times \nabla(\mathcal{L}^{-1}(q_l{}')) \qquad \text{(7a, 7b)}$$

205

206 Equation (6) shows the terms that contribute to the upper layer (500-50mb) QG height
207 tendencies only; six additional terms of similar form can be determined for the low-level QG
208 height tendency field. Term A represents the advection of upper level perturbation QGPV, $q_u{}'$,
209 by the background geostrophic winds $\overline{\boldsymbol{v}}_g$. This term includes effects from the advection,
210 deformation, and superposition of anomalies by the background flow (Fig.2). The mean wind
211 will always tend to advect disturbances downstream, which leads this term to be high in
212 magnitude and also flank the sides of the anomaly (Fig.2a). Development can occur due to
213 asymmetry in the mean state, often manifested as confluence or diffluence (Fig.2b). The shape
214 of a PV anomaly situated in an asymmetric background state can be rearranged, changing its
215 attendant circulation. If the feature becomes more isotropic, the circulation will strengthen, and
216 vice versa. The effect from the horizontal and vertical overlapping of QGPV anomalies, which
217 may be brought together by the mean flow to superpose, is also included in Term A (horizontal
218 example, Fig.2c). Term A will be referred to as the deformation/superposition term.
219 Term A has a barotropic component which can be isolated by setting the winds from
220 1000-50 hPa equal to their value at 300mb, and inverting the resultant advection. Doing so
221 eliminates any advection caused by vertical wind shear that may exist in the background state,
222 effectively prescribing the wind field to be barotropic. Height tendencies that remain after taking
223 the difference between the unpartitioned $\overline{\boldsymbol{v}}_g$ wind field and this barotropic component are
224 attributed to vertical wind shear. Vertical shear can differentially advect anomalies so that they
225 vertically overlap and strengthen the circulation of a particular feature, inducing growth. NGL

consider development associated with this component of Term A to be a sign of transient, 'nonmodal growth'. Transient growth occurs when the tilt of anomalies with height changes over time, leading to the vertical overlapping of anomalies of the same sign ('modal' growth such as in the Eady problem involves a fixed tilt with height over time).

Term B represents the advection of upper level background QGPV, $\overline{q}_u$, by the circulation associated with upper level QGPV anomalies, $\boldsymbol{v}'_{gu}$. This term can be important at the leading edge of a wave packet, where individual waves have different amplitudes, leading to asymmetric $\overline{q}_u$ advection such that the waves at the front of the packet grow due to the effect of higher-amplitude anomalies upstream (Fig. 3). NGL found that this term contributed to the early stages of development of an upper-level trough in their case, and interpreted this development as resulting from Rossby wave energy propagating into the area from upstream, at the leading edge of a wave packet. By virtue of these allusions to downstream development or group velocity effects, we refer to this term as the downstream development term, following NGL.

Term C represents the effect of low-level perturbation QGPV, $q_l{}'$, and its associated tropospheric- deep circulation, on $\overline{q}_u$. Given favorable phasing (ie, westward tilt with height) between upper- and lower-layer anomalies, the circulation associated with a low-level feature (such as a surface cyclone) can advect $\overline{q}_u$ and amplify a disturbance in the upper troposphere. Simultaneously, the circulation associated with the upper-level feature amplifies the lower-level one, and both features develop. Accordingly this term is commonly interpreted as including effects from baroclinic development. Terms D and E represent nonlinear interactions between the upper and lower-level anomalous geostrophic circulations and QGPV features, and depend heavily upon the geometry of the flow field. These two terms involve the anomalous circulation ($\boldsymbol{v}'_{gu}$ *or* $\boldsymbol{v}'_{gl}$) rearranging $q_u{}'$, and are considered vortex-vortex interaction terms.

249 Overrelaxation techniques are employed to solve for the tendencies associated with each
250 term, which can be linearly combined to arrive at the overall piecewise QG tendency. Finally, to
251 confirm that the QG height tendency components are representing the 'observed' development of
252 ϕ_u', the height tendency values from the sum of all piecewise terms (6) are compared against the
253 centered finite-differenced approximation to $\frac{\partial \phi_u'}{\partial t}$ using the ϕ_u' field (8), after all fields were
254 smoothed with a 25-point smoother.

255 $$QG_{obs} = \frac{\phi_u'(t+1) - \phi_u'(t-1)}{2dt} \quad (8)$$

256 PTD is applied to an important feature associated with the initiation of an extreme jet retraction
257 that began in mid-February 2006. The basic/mean/background state is defined as the five-day
258 time mean from 11-15 February 2006, the period just prior to retraction onset. After an overview
259 of the case is presented in Section 3, results from PTD are shown in Section 4.

260 **3. Synoptic Overview**

261 The north Pacific jet retraction that began in mid-February 2006 was related to a period
262 of extreme rainfall over Hawaii that continued throughout March (Table 1 Jaffe et al. 2011;
263 Jayawardena and Chen 2011). The Federal Emergency Management Agency (FEMA) declared
264 the event a natural disaster due to the resultant flooding, mudslides and damages (FEMA Case
265 #1640). The rapid onset of the precipitation broke a dry spell over Hawaii that had been
266 associated with an extended jet (Climate Prediction Center). A synoptic overview of that
267 initiation of this event is given in terms of tropopause maps and Hovmöller diagrams.

268 *a. Tropopause Maps*

269 Consideration of potential temperature on the 2 PVU surface, the dynamic tropopause,
270 presents a succinct overview of the upper-tropospheric dynamical evolution (Morgan and
271 Nielsen-Gammon 1998) and forms the basis of the analysis of the five days leading up to

retraction (Figs. 4-6). A positive θ anomaly on the 2PVU surface represents an anticyclonic anomaly, while a negative θ anomaly signifies anomalous cyclonic flow. Figure 4 shows the 1979-2016 February mean, with three θ contours highlighted. The strong west Pacific jet stream is evident where the meridional θ gradient is strongest, while its exit region is indicated by the diffluence of the θ contours near 160°W. Higher θ values are present in the subtropics, signifying a higher, potentially warmer tropopause. Values of θ decrease moving poleward, in some places over a short distance, indicating where the tropopause slopes dramatically and wind speeds are highest (as in the west Pacific). A lower, potentially colder tropopause is observed at higher latitude.

Daily mean θ anomalies, along with the 315, 330 and 345 K contours, are shown in Figs. 5-6. Beginning on 11 February, a strong, zonally extended jet reaches 160°W as implied by the tight and zonally oriented θ gradient (Fig.5a). Two high-amplitude ridges characterized by positive θ anomalies bookend the jet, one upstream of the jet entrance region labeled B, the other located downstream over northwestern Canada and Alaska. A small, zonally-elongated positive θ anomaly was situated within the jet over southern Japan, labeled A. Feature A develops rapidly into a high-amplitude, large-scale, wavenumber 3 ridge by 15 February (Fig.5b-e). A's emergence from the subtropics into the midlatitudes first displaces the jet exit region westward and initiates the weakening of the jet by diverting the 315K contour northward as it grows, weakening the θ gradient on the dynamic tropopause and thus the tropopause-level geostrophic wind.

During this time, B moves southeastward, its shape changing from nearly circular on 11 February to zonally elongated by 13 February as the anomaly is deformed first by confluence in the jet entrance and then by the strong winds in the jet core. Feature A becomes stationary on 15

295 February and acquires a positive tilt the next day (Fig.5f), signifying the beginning of an
296 anticyclonic/LC1 wave break over western North America[2]. Finally, we note that from 14-16
297 February, B hardly moved, remaining situated within the jet and maintaining its oblong shape.
298 15 February is the first day on which the Jaffe et al. (2011) jet retraction criteria were met,
299 coinciding with when A was strongest. By 16 February, a trough-like feature had developed in
300 the subtropics northwest of Hawaii at 330-345K.

301 Figure 6 shows the θ evolution from 17-27 February, now skipping every other day for
302 brevity. On 17 February, A overturned, as its base remained in the eastern Pacific with its crest
303 farther downstream over the Canadian archipelago. B was located near the date line and was
304 more isotropic than one day earlier (Fig.6a vs Fig.5f). Two days later (Fig.6b) A and B had
305 merged, as B encroached upon the nearly stationary A. The deformation associated with the jet
306 exit region was, by this time, located near 160°E, a combined result of the evolution of A and the
307 emergence of B out of the jet core. The subtropical central Pacific remained characterized by a
308 potent, stationary trough on 330-345K throughout the ten-day period. The trough diverted flow
309 southward in the central Pacific, and, in concert with the ridge to its north, enhanced the
310 deformation. The development of the subtropical trough also coincided with the beginning of the
311 rainy period over Hawaii (Jayawardena and Chen 2011; Climate Prediction Center).

312 Yet another midlatitude anticyclonic anomaly, C, emerged over Japan on 21 February,
313 rapidly developing and overturning two days later (Fig.6c-d). The resultant anticyclone
314 remained through 25 February (Fig.6e). The attendant split flow, with one branch diverted north
315 of C and the other to the south of the subtropical cyclone, persisted through 27 February, by
316 which time the meridional θ gradient was extremely weak throughout most of the basin.

[2] Pelly and Hoskins (2003) showed that wave breaking can be identified when the meridional θ gradient reverses, as seen in the 315K contour on the 16th.

317 Considering the two-week period overall, the transition of the large-scale circulation from a
318 strong, zonal jet to this split, wavy flow is rather stark.
319 To summarize, five days prior to retraction the jet was strong and zonal, and was
320 subsequently split due to A and B, which both displaced the 315K contour northward and
321 reduced the meridional tropopause potential temperature gradient on the dynamic tropopause.
322 Both A and B halted in the east-central Pacific in regions of extreme deformation, and were
323 associated with a period of anticyclonic wave breaking on 315K at rather high latitude and low
324 altitude (low θ). To the south of these two anticyclonic features, stationary cyclonic anomalies
325 developed in the subtropics, repeatedly inundating Hawaii with heavy precipitation. At times, the
326 330K contour overturned cyclonically northwest of Hawaii while the 315K contour wrapped up
327 anticyclonically to its north (Fig.6d).
328 *b. Hovmöller*
329 A succinct overview of the flow transition associated with the jet retraction is evident in
330 Hovmöller diagrams of 300hPa standardized height anomalies averaged over 20-30°N and 40-
331 50°N (Fig.7). In the subtropics (Fig.7a), the first half of February is characterized by higher than
332 normal heights from about 130°-180°E, which are then replaced by negative, cyclonic anomalies
333 after 15 February for the remainder of the month and much of March. These low height
334 anomalies are centered near the date line and coincide with the persistent, heavy precipitation
335 over Hawaii. Also of note is how stationary the anomalies are, reflective of the dipole-type
336 block. The midlatitude region (Fig.7b) in early February is characterized by many progressive
337 systems as evidenced by cyclonic anomalies moving quickly from west to east over a short
338 period of time. The high-amplitude ridge observed on 11 February at 240°W (Fig. 5a) is seen to
339 form and stay in place from 5-11 February, when the jet is extended. Thereafter, 'A' forms

farther upstream at 200°E and similarly ceases to propagate as observed on the tropopause maps. 'B' is also evident, emerging out of the east as a +2 standard deviation anomaly on 11 February, moving eastward while 'A' remains at 200°E.

After the 15 February the formation of C heralds the beginning of a long-lived block that persists until about 5 March. The sprawling and potent anticyclonic anomaly is contemporaneous with cyclonic anomalies in the subtropics, the two forming a dipole-type block, which maintains a retracted jet. It is of interest that the midlatitude anticyclone is far more expansive zonally (120-200°E) than the subtropical cyclonic feature (160-190°E), indicating that the wavelengths of the two stationary features are rather different.

Later in March, the subtropics experienced another period of lower than average heights that remained fixed between 180°-200°E for 15 days. The stationary nature of the anomalies is similar to the earlier period just discussed. Interestingly, the attendant midlatitude behavior differs from the sprawling, blocked anticyclone that occurred in late February-early March. Rather, a series of progressive ridges interspersed with weak troughs occupies the basin during the latter period, with only one instance of quasi-stationary growth around 15-22 March.

c. EOF1 and the Pacific-North American Pattern

One final perspective is presented to investigate the large-scale flow transition associated with this jet retraction and how it is related to the PNA. Figure 8 shows the 250mb zonal wind EOF1 pattern overlaid with the mean jet position (contours Fig. 8a) and its corresponding PC1 time series, along with the PNA index for February-March 2006 (Fig. 8b). The phase of the jet as expressed by this EOF on a given day can be determined by multiplying the value of PC1 on that day by the pattern in Fig.8a. For example, from 10-12 February PC1 is positive, indicating that the jet is extended (confirmed by inspection of Fig. 5a). The PNA index is also positive at this

363 time. Thereafter, PC1 rapidly decreases and reaches values of -3-4σ, reflecting the extreme
364 retraction that occurred. The PNA index also becomes substantially negative, although while
365 PC1 decreases to -3σ before 20 February, the PNA reaches its minimum value one week later,
366 near the end of February (see blue and red stars in Fig.8b). Clearly, there is very good
367 correspondence between the transition of the jet from extended to retracted and the development
368 of the negative PNA phase. Modification of the jet therefore seems important for maintenance
369 and amplification of the negative PNA pattern.

370 **4. Piecewise Tendency Diagnosis**

371 Since the chain of events that led to the prolonged retraction event was initiated by the
372 growth of Feature A, in this section the development of Feature A is diagnosed from the QG
373 height tendency perspective using PTD.

374 *a. Evaluation of QG Diagnosis*

375 The 300mb geopotential height anomalies retrieved from inverting the perturbation
376 QGPV, split into two levels using (2b), very closely match those calculated directly using ERA-
377 Interim geopotential. The ERA-interim geopotential anomaly will be referred to as ϕ'_a. Figure 9
378 shows time series tracking the contribution to the maximum height value associated with Feature
379 A using the three height fields[3], ϕ'_u, ϕ'_l, and ϕ'_a. The sum of the upper and lower layer
380 contributions adds up to the pink line, ϕ'_{tot}. The extremely close match between the Reanalysis
381 anomaly ϕ'_a (blue dash), and ϕ'_{tot}(pink), confirms the inversion method was successfully
382 implemented, and shows that both fields undergo substantial development into a 300+ meter
383 ridge during the five day period.

[3] At 06z, 12z 11 February, a distinct height anomaly associated with A has not yet developed as shown in Fig.9b. Instead of tracking the position of maximum ϕ_{tot}, the grid point of most positive height tendencies, using the QG_{obs} field, in the region from which Feature A emerges, (marked by the A in figure 9b) is used. In this way, it is still possible to diagnose the initial development of Feature A.

From 11-13 February, ϕ'_u accounts for most of the upper level ridge (ϕ'_{tot}), while a substantial contribution on the order of 100m comes from ϕ'_l starting at 12z on the 14th, indicating a low-level ridge has developed and is located directly underneath Feature A at upper levels. To illustrate the evolution of the vertical structure of the circulation near A, Fig. 10 shows the 300hPa and 950hPa ϕ'_{tot} fields in black and red, respectively, at 12-hour intervals from 00z 13 February – 00z 15 February. At 00z 13 February, Feature A is amplifying, while a 950hPa anticyclone is beginning to develop to the east of A (labeled H), indicating a characteristic westward tilt with height (Fig. 10a). The 300hPa trough and surface cyclone upstream of A also exhibit westward tilt with height. Over the next 36 hours, the 950hPa ridge amplifies and remains rather stationary, while A amplifies but moves eastward (Fig. 11 b-d). By 12z 14 February, the anticyclones are vertically stacked in the east Pacific, and remain so at 00z 15 February. The implications of the change in the vertical structure of feature A from baroclinic to equivalent barotropic will be discussed in section 4b. However, as the ϕ'_u field accounts for the majority of the total 300mb ridge during its development period from 11-13 February, PTD is applied to diagnose the development of the upper-level ridge using (6).

Confirmation that the observed height tendencies, approximated by the finite-difference of the ϕ'_u field, (Eqn (8)), are reasonably represented by the sum of the QG piecewise terms (Eqn (6)) is given in Fig.11. When positive (negative) height tendencies are observed, development (decay) of the ridge is anticipated. The two methods of determining height tendencies, Eqn (6) and Eqn (8) both indicate that there were positive height tendencies over Feature A until 00z 14 February, reflecting the rapid development that was observed in the synoptic overview. Overall there is very good agreement between the observed and QG height tendencies, although the QG, piecewise sum sometimes overestimates development or decay. The two time series shown in

Fig. 11 have a correlation of 0.90, and overall the temporal evolution and general magnitude of amplification match quite well. The processes represented by the QG height tendencies therefore account for the majority of the observed growth of Feature A.

b. Components of QG Height Tendencies

In this section, the terms driving development of Feature A through its initial growth period on the 11th, sustained growth thereafter and subsequent weakening will be investigated. Negative PV advection into the center of Feature A drives height rises and amplification and was achieved via several processes during A's lifecycle. First, southerly flow on the eastern side of a deep, high-PV intrusion advected low background PV northward, producing a positive height anomaly, A, on 11 February. Next, upper-level deformation and superposition, as well as effects from a strong surface cyclone, continued to amplify Feature A through continued negative PV advection, from 12-13 February. Decay of Feature A begins on 14 February and was driven by the deformation term, which began to advect *high* PV into the ridge center, leading to height falls over A.

i Initial Growth of Feature A from a PV intrusion

As previously noted, Feature B, a high-amplitude ridge located on the tropopause over Eurasia, reached the poleward side of the jet entrance region on 11 February, and overturned anticyclonically. Figure 12a shows the perturbation QGPV at 12z 11 February, with B labeled. Downstream of B, a potent, positively tilted 300hPa trough developed (also evident in Fig. 9b), and a cross section averaged from 130-140°E shows that the trough was linked to a deep intrusion of anomalous high-PV air into the troposphere to 750hPa (Fig.12b). The high-PV intrusion tilted southward and crossed the upper-level jet axis, and corresponding $\nabla\overline{q}$, which is shown in Fig. 12c. The total QGPV (i.e., sum of fields in Fig. 12b and Fig. 12c) indicates the

position of the PV intrusion with respect to the strong 300hPa $\overline{\nabla q}$ and the jet. Southerly flow on the intrusion's eastern side (arrows Fig. 12 b, d) was positioned to advect low PV northward, inducing positive height tendencies and development of A.

Inverting q_l' between 550-750hPa isolates the PV intrusion and its associated height field, which will be referred to as ϕ'_{l_intr}. Figure 13a-b shows the ϕ'_{l_intr} field at 300hPa in contours, with the background QGPV in the fill, at 12z and 18z 11 February. The negative height anomaly associated with the PV intrusion was centered over southern Japan, and southerly winds on the intrusion's eastern side crossed the strong background QGPV gradient, transporting low PV northward. Inverting the baroclinic development term, $-\mathbf{v}'_{\mathrm{gl}} \cdot \overline{\nabla \mathrm{q}}_{\mathrm{u}}$, using winds associated *only* with ϕ'_{l_intr} produces positive height tendencies in the location of negative PV advection in a broad region to the east of Japan from about 25-55°N. The southern extent of the positive height tendencies in the subtropics is the location from which Feature A emerges by 18z on the 11th (Fig.13c-d).

The circulation associated with the upper-level trough that is located upstream of A, and is linked to the PV intrusion just discussed, also plays a role in A's initial development. Similar to the mid-tropospheric PV intrusion, on 11 February, southerly flow on the upper-level trough's eastern side advected low background PV northward in generally the same region as the PV intrusion (negative height anomaly in Fig. 12c-d). The downstream development term $(-\mathbf{v}'_{\mathrm{gu}} \cdot \overline{\nabla \mathrm{q}}_{\mathrm{u}})$, captures the height tendencies associated with this upper level influence on the background QGPV. The time series of height tendencies associated with advection caused by the upper level trough and PV intrusion, evaluated at Feature A's ϕ'_{tot} maximum, are shown in Fig. 14. The baroclinic term (550-750hPa component of Term C in Eqn(6)) and the downstream development term (Term B Eqn (6)), both contribute notably to the growth of A on 11 February.

453 The influence of the PV intrusion weakens but remains positive through 12-13 February, while
454 the downstream development term opposes development after 12z 11 February.
455 *ii. Prolonged Growth of Feature A Via Upper-level Deformation & Superposition, and a Surface*
456 *Cyclone*
457 The upper-level trough and PV intrusion also led to the development of a surface cyclone
458 that amplified in the central Pacific from 12-14 February (see Fig. 11, red dashed contours). The
459 surface cyclone was located upstream of A and downstream of the upper-level trough from 00z
460 13 February – 00z 14 February. The height field attained by inverting q_l' from 1000-800hPa
461 only, ϕ'_{l_sfc} isolates the influence of the surface cyclone, which extends throughout the
462 troposphere. The cyclone's circulation was strong enough, and positioned in such a way, that
463 southerly flow on its eastern side crossed the strong 300hPa background PV gradient associated
464 with the jet (arrows in Fig. 15a). The resultant negative $\overline{\mathrm{q}}_\mathrm{u}$ advection promoted A's growth in a
465 manner similar to that of the streamer and upper-level trough on the 11 February. Inverting the
466 baroclinic development term ($-\mathbf{v}'_{\mathrm{gl}} \cdot \nabla\overline{\mathrm{q}}_\mathrm{u}$) using only the circulation due to ϕ'_{l_sfc} yields the
467 height tendency response due to the surface cyclone, showing strong positive height tendencies
468 overlapping with A (Fig.15b). Figure 16 shows the temporal evolution of the height tendency
469 contribution to Feature A's growth from the 1000-800hPa component of the baroclinic
470 development term. Height rises from this term show the cyclone contributes strongly and
471 consistently to development of A until 14 February. After this time, the cyclone is diverted
472 northward, away from the strong, 300hPa background PV gradient (Fig. 11d-e).
473 In addition to the surface cyclone, upper-level deformation and superposition strongly
474 contribute to amplification of Feature A from 00z 12- 12z 13 February. The
475 deformation/superposition term, $-\overline{\mathbf{v}}_\mathrm{g} \cdot \nabla \mathrm{q}'_\mathrm{u}$, captures the effect of the background circulation

476 advecting and reorganizing upper-level QGPV anomalies, including Feature A. High-amplitude
477 deformation is evident in the mean state jet exit region (contours, Fig.17a), leading the
478 background winds to modify the shape of Feature A, in a manner suggested by the schematic in
479 Fig. 2b. Figure 17a shows the q_u' field at 00z 13 February along with the background
480 geopotential height contours, from which $\overline{\mathbf{v}}_g$ can be discerned. At this time Feature A was
481 situated in between strong, zonal flow on its western side and weak, northward-diverted flow on
482 its eastern side. The position of A in the deformation region is similar to the PV anomaly in the
483 schematic in Fig. 2b. The modification of A's shape by the mean flow increased A's isotropy at
484 this time, evidenced by height rises due to the deformation/superposition term overlap with the
485 center of Feature A (Fig. 17b). The temporal evolution of the deformation/superposition term
486 shows that deformation amplifies A during its most rapid development period, 12-13 February
487 (Figure 18). A further partition of this term shows that the *barotropic* component, which
488 captures the effect of horizontal deformation, most strongly amplifies Feature A. The barotropic
489 component changes sign and promotes A's decay, starting at 18z 13 February, discussed in the
490 next sub-section.

491 A positive contribution from the *non-modal* component of Term A to intensifying Feature
492 A is observed in Fig. 18 from 00z 12 February – 12z 14 February. This indicates that, in
493 addition to horizontal asymmetry in the mean state, vertical shear in the mean state rearranged
494 the three-dimensional q_u' field in a manner conducive to A's development. This component of
495 the deformation/superposition term contributed to A's growth during the period when the vertical
496 tilt between upper- and lower-levels evolved from westward tilted to vertically stacked (Fig. 11b-
497 e). The vertical superposition of the upper- and lower-level anticyclones, brought together by the
498 vertical shear in $\overline{\mathbf{v}}_g$, evidently occurred during this period. Once the upper- and lower-level

anticyclones became vertically stacked by 12z 14 February, this term no longer promoted development of Feature A (Fig. 11d-e).

iii. Decay of Feature A

As Feature A propagates further into the region of deformation in the eastern Pacific, the direct effect of deformation transitions from strengthening to weakening A, as observed in the time series in Fig. 18. Feature A, and the trough upstream of A, propagate eastward with time, and positive q'_u advection associated with the upstream trough strengthens and encroaches on Feature A. By 00z 14 February, the background geostrophic wind reorganizes q'_u such that A becomes *less* isotropic and its circulation is attenuated (Fig. 19a). Simultaneously, there is strong *positive* q'_u advection on A's upstream side, associated with the upstream trough. The associated positive q'_u advection by $\overline{\mathbf{v}}_g$ overlaps with the center of Feature A, inducing height falls and weakening A on the 14th, evident in Fig. 19b.

iv. PTD Summary

The cumulative effect of all processes that contribute to the QG height tendencies associated with Feature A is summarized in Fig.20, which shows time series of all components in (6). First an upper-level trough and its deep PV intrusion initiated development and created a distinct positive height anomaly through negative $\overline{q}_u$ advection on its eastern edge (dark blue line). Thereafter, effects from tropopause-level deformation, vertical shear, and a strong surface cyclone cause continued and intense amplification by importing low-PV into Feature A (green, light blue lines, respectively). Overall a lifecycle emerges wherein downstream development associated with the leading edge of a wave packet, including a tilted, deep PV intrusion, initiates growth and creates a positive height anomaly in the subtropics on the equatorward side of the jet. Thereafter, effects from a deformed tropopause and a strong surface cyclone drive development,

522 including a contribution to growth related to vertical shear in the mean state. Feature A
523 propagates northeastward along $\overline{\nabla q}_u$ as it amplifies, splitting the jet as it propagates, evident in
524 Fig.5c-d. Decay of A is driven by deformation as well, which begins to attenuate the q'_u anomaly
525 associated with Feature A rather than consolidate it, leading to a weaker anticyclonic anomaly.

526 **5. Discussion and Conclusions**

527 This study investigated an extreme jet retraction in the north Pacific that transformed the
528 circulation in this basin from one characterized by a progressive storm track and a strong zonal
529 jet, to a split, blocked flow in mid-February and March 2006. Retraction onset preceded the
530 development of a long-lived negative PNA pattern. The initiation of this jet retraction is
531 associated with the lifecycles of two key anomalies, A and B, that divert and retract the jet
532 through serial LC1 wavebreaking events, mostly confined between 315-330K and occurring in
533 regions of strong deformation. The lifecycle of the first wave to break anticyclonically is
534 diagnosed within a QG piecewise tendency framework, and confirms the physical connections
535 between jet variability, Rossby wave breaking, and the PNA teleconnection pattern revealed in
536 prior studies.

537 NGL found that downstream development contributed to the amplification of an upper-
538 level mobile trough very early on in the trough's lifecycle, when a Rossby wave packet, and its
539 associated energy, propagated into the region from the west. Baroclinic development drove the
540 majority of development of the trough thereafter, while effects from deformation were variable
541 and minimal. Evans and Black (2003) used PTD to diagnose persistent (>7day duration) 500hPa
542 anticyclonic anomalies in the North Pacific, the closest analogue to Feature A that has been
543 diagnosed with PTD. During the most rapid development period of the anticyclones they
544 identified, 90% of intensification was associated with baroclinic growth, the other 10% with

545 deformation. Downstream development drove decay of anticyclones in this study, similar to
546 results in NGL, and at no point did this term aid in growth of persistent, 500hPa anticyclones.
547 In the case presented here, deformation exerts a dominant influence on the growth *and*
548 decay of Ridge A, a result that has not been observed in the Pacific region before. Additionally,
549 the downstream development opposed the effect of deformation, promoting growth when the
550 ridge decayed, in direct opposition to the results of both NGL and Evans and Black (2003) (Fig.
551 20 dark blue line).
552 The mean-state deformation is collocated with a weak meridional QGPV gradient (Fig.
553 21), which is proportional to the zonal phase speed (c_x) of a two-dimensional Rossby wave (8),
554 where *k* and *l* are the zonal and meridional wave numbers, respectively.

555 $$c_x - \bar{u} = -\frac{\frac{\partial \bar{q}}{\partial y}}{(k^2+l^2)} \qquad (8)$$

556 As Feature A propagates into the region of weak $\nabla\overline{q}_u$, $\bar{u}$ and its phase speed decrease rapidly,
557 and A becomes stationary by 15 February. The downstream development term captures the
558 effect of Rossby wave energy propagation, which is also proportional to the meridional gradient
559 of $\overline{q}_u$. As a result the group velocity is weakened as it reaches the weak $\overline{\nabla q}_u$ in the mid-latitude
560 east Pacific. In this case, the change in sign of the downstream development term between 13
561 and 14 February, coincident with A reaching the region of strong deformation/weak $\nabla\overline{q}_u$, is a
562 sign that energy is blocked from propagating downstream by the deformation region. Time
563 series of the deformation and downstream development terms from 11-15 February are
564 negatively correlated (r=-.77), another suggestion that the two terms are governed by the same
565 characteristic of the environment: the deformation region. This inverse relationship between

566 deformation and downstream development's influence on growth has not been found by previous
567 studies employing PTD.

568 Mak and Cai (1989) discussed how the shape and orientation of eddies with respect to
569 deformation influences the barotropic energy exchange between eddies and the background state
570 kinetic energy. A positively-tilted trough in a region of cyclonic shear is conducive to trough
571 intensification as energy is extracted from the background. The trough upstream of A on 11
572 February (see Fig. 9b) is in such an environment, suggesting barotropic growth was occurring
573 within the vicinity of A. Indeed, Evans and Black (2003) interpreted growth from the barotropic
574 deformation term in the PTD framework as evidence of barotropic growth, which they found was
575 important for developing cyclones and anticyclones in the Atlantic region. The lifecycle of
576 Feature A, dominated by the deformation term, provides additional evidence for a connection
577 between a positively tilted wave structure, barotropic growth, and finally, a weakened zonal jet.

578 Shutts (1983) demonstrated how deformation associated with a block led to a vorticity flux
579 forcing on the zonal wind that maintained the block. His Fig.1 shows how eddies approaching
580 the deformation and block are stretched out and weakened within the block themselves, as
581 observed in this case on 14 February. It is shown through PTD that this process can be captured
582 through a change in sign of the deformation and downstream development terms, and the
583 coincidence of deformation both weakening the ridge by stretching it out *and* preventing the
584 downstream propagation of Rossby wave energy.

585 Returning to consideration of the composite flow evolution during jet retractions (Fig.1),
586 many previously elusive features can now be placed in an emerging dynamical context. An
587 extended jet accompanied by a high-amplitude ridge in the exit region sets up an environment
588 conducive to initiating a retraction by forming a region of strong deformation. The negative PV

589 anomaly on the cyclonic shear side of the jet in the composite, B in this case, encounters the jet
590 entrance region, at which point it initiates a positively-tilted, southeastward-directed wave train,
591 leading to the growth of a ridge, Feature A, in the subtropics. A's subsequent development
592 marks the beginning of the disruption of the zonal jet. Meanwhile, the subtropical waveguide
593 (345K, Figs. 5-6) is displaced southward and is characterized by a strip of synoptic-scale,
594 cyclonic PV anomalies to the south of the sprawling anticyclone, accounting for the zonally-
595 extended but meridionally confined cyclonic PV anomaly observed in the composite. This
596 subtropical component represents the southern branch of the split flow observed during Rex
597 blocking events, and in this case was related to a period of unprecedented rainfall over Hawaii.
598 Preliminary diagnosis of other jet retractions indicates the role of deformation is common among
599 the extreme jet retractions identified by Jaffe et al. (2011), and future work will focus on
600 complementing them with zonal wind tendency diagnostics, as well as investigate the
601 predictability of retractions and the dipole-type blocking that follow their development.
602
603
604

605
606 REFERENCES

607 Athanasiadis P. J., J. M. Wallace, and J. J. Wettstein, 2010: Patterns of wintertime jet stream
608 variability and their relation to the storm tracks. *J. Atmos. Sci.,* **67,** 1361-1381,
609 doi:10.1175/2009JAS3270.1.

610

611 Charney, J. G. and M. E. Stern, 1962: On the stability of internal baroclinic jets in a rotating
612 atmosphere. *J. Atmos. Sci.,* **19**, 159-172.

613

614 Davis, C., and K. A. Emanuel, 1991: Potential vorticity diagnostics of cyclogenesis. *Mon.*
615 *Wea. Rev.,* **119,** 1929-1953.

616 Dee, D. P., S. M. Uppala, A. J. Simmons, P. Berrisford, P. Poli, S. Kobayashi, U. Andrae, M. A.
617 Balmaseda, G. Balsamo, P. Bauer, P. Bechtold, A. C. M. Beljaars, L. van de Berg, J.
618 Bidlot, 5. N. Bormann, C. Delsol, R. Dragani, M. Fuentes, A. J. Geer, L. Haimberger, S.
619 B. Healy, H. Hersbach, E. V. Hólm, L. Isaksen, P. Kållberg, M. Köhler, M. Matricardi,
620 A. P. McNally, B. M. Monge-Sanz, J.-J. Morcrette, B.-K. Park, C. Peubey, P. de Rosnay,
621 C. Tavolato, J.-N. Thépaut and F. Vitart, 2011: The ERA-Interim reanalysis:
622 configuration and performace of the data assimilation system. *Quart. J. Roy. Meteor.*
623 *Soc*., **137-656**, Part A, 553–597. DOI: 10.1002/qj.828.

624 Dole. R. and N. D. Gordon, 1983: Persistent anomalies of the extratropical Northern Hemisphere
625 wintertime circulation: Geographical distribution and regional persistence characteristics.
626 *Mon. Wea. Rev.,* **111,** 1567–1586.

627 Eady, E. T., 1949: Long waves and cyclone waves. *Tellus*, **1 (**Part **3),** 33-52**.**

628 Eichelberger, S. J., and D. L. Hartmann, 2007: Zonal jet structure and the leading mode of
629 variability. *J. Climate*, **20**, 5149– 5163.

630 Evans, K. J. and R. X. Black, 2003: Piecewise tendency diagnosis of weather regime transitions
631 . *J. Atmos. Sci.,* **60**, 1949-1959.

632 FEMA: https://www.fema.gov/disaster/1640#tabs-2

633

634 Fleming, E. L., G.-H. Lim, and J. M. Wallace, 1987: Differences between the spring and autumn
635 circulation of the Northern Hemi- sphere. *J. Atmos. Sci.,* **44,** 1266–1286.

636 Franzke C, Feldstein SB, Lee S (2011) Synoptic analysis of the Pacific-North American
637 teleconnection pattern. *Quart. J. Roy. Meteor. Soc* **137**, 329–346.

638 Griffin, K. S., and J. E. Martin, 2017: Synoptic features associated with temporally coherent
639 modes of variability of the north Pacific jet stream. *J. Climate*, **30**, 39-54.

640

641 Jaffe, S. C., J. E. Martin, D. J. Vimont, and D. J. Lorenz, 2011: A synoptic-climatology of
642 episodic, sub-seasonal retractions of the Pacific jet. *J. Climate*, **24**, 2846-2860.

643

644 Jayawardena, I. M and Y. L. Chen, A. J. Nash, K. Kodama, 2012: A Comparison of three
645 prolonged periods of heavy rainfall over the Hawaiian Islands. *J. Appl. Meteor.,* **51**, 722-
646 744.

647

648 Mak, M., and M. Cai, 1989: Local barotropic instability. J. Atmos. Sci., **46,** 3289–3311.

McIntyre, M.E. and T. N. Palmer, 1983: Breaking Planetary waves in the stratosphere. *Nature*, **305**, 593-600.

Namias, J. and P. F. Clapp 1949: Confluence theory of the high tropospheric jet stream. *J. Meteorology*, **6**, 330-336.

NCEP Reanalysis 2: *Boulder, Colorado, USA, from their Web site at http://www.esrl.noaa.gov/psd/*

Newman, M., and P. D. Sardeshmukh, 1998: The impact of the annual cycle on the North Pacific/North American response to remote low-frequency forcing. *J. Atmos. Sci*., **55,** 1336–1353.

Nielsen-Gammon, J. W. and R. J. Lefèvre, 1996: Piecewise Tendency Diagnosis of Dynamical Processes Governing the Development of an Upper-Tropospheric Mobile Trough. *J. Atmos. Sci.,* **53**, 3120–3142.

Otkin, J. A., and J. E. Martin, 2004. The large-scale modulation of subtropical cyclogenesis in the central and eastern Pacific Ocean. *Mon. Wea. Rev.*, **132**, 1813-1828.

Palmén, E. (1948). On the distribution of temperature and winds in the upper westerlies. *J. of Meteorology,* **5**, 20-27.

672

673 Palmén, E. and Newton 1969: *Atmospheric circulation systems.* Academic Press., **13,** 606.

674 Pelly, J. L. and B. J. Hoskins, 2003: A new perspective on blocking. J. Atmos. Sci., **60**, 734-755.

675

676 Rex, D. F., 1950: Blocking action in the middle troposphere and its effect upon regional climate.
677 *Tellus*, **2-3**, 196-211.

678

679 Shutts, G. J., 1983: The propagation of eddies in diffluent jetstreams: Eddy vorticity forcing of
680 ‘‘blocking’’ flow fields. *Quart. J. Roy. Meteor. Soc*., **109**, 737–761.

681

682 Simmons, A. J. and B. J. Hoskins 1980: Barotropic influences on the growth and decay of
683 nonlinear baroclinic waves. *J. Atmos. Sci.,* **37,** 1679-1684

684

685 Thorncroft, C. D., B. J. Hoskins and M. E. McIntyre, 1993: Two Paradigms of Baroclinic-wave
686 life-cycle behavior. *Quart. J. Roy. Meteor. Soc.* **119,** 17-55.

687

688 Wallace, J. M. and D. S. Gutzler, 1981: Teleconnections in the Geopotential Height Field during
689 the Northern Hemispher Winter. *Mon. Wea. Rev.,* **109**, 784-812.

690

691 Weickmann, K. M., and R. M. Chervin, 1988: The observed and simulated atmospheric seasonal
692 cycle. Part I: Global wind field modes. *J. Climate,* **1,** 265–289.

693

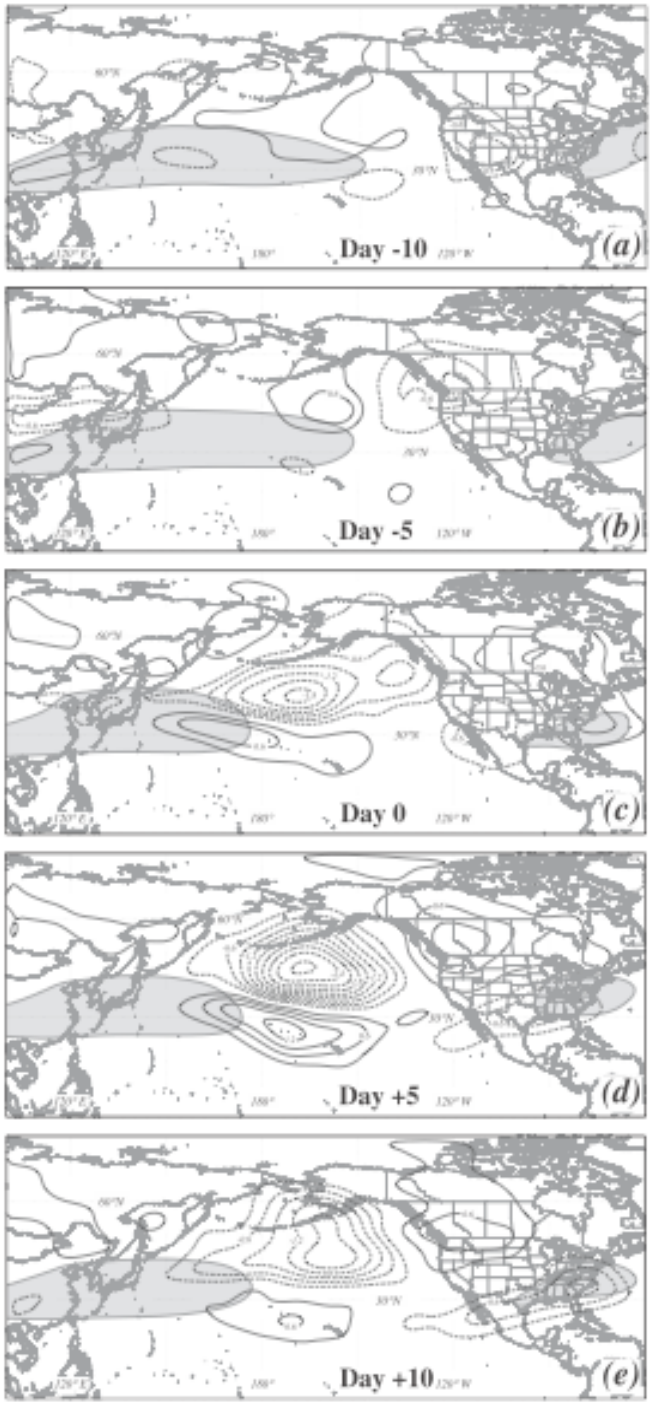

Figure 1: Adopted from Jaffe et al. (2011). Composite 200-250-hPa Ertel Potential Vorticity anomalies associated with a jet retraction event at days (a) -10, (b) -5, (c) 0, (d) +5, and (e) +10. Solid (dashed) lines indicated positive (negative) perturbation PV, contours every 0.3 PVU (1PVU = 10^{-6} m^2 K kg^{-1} s^{-1}) with the 0 line removed. Grey shading represents the 40 ms^{-1} isotach of the composite 250-hPa zonal wind.

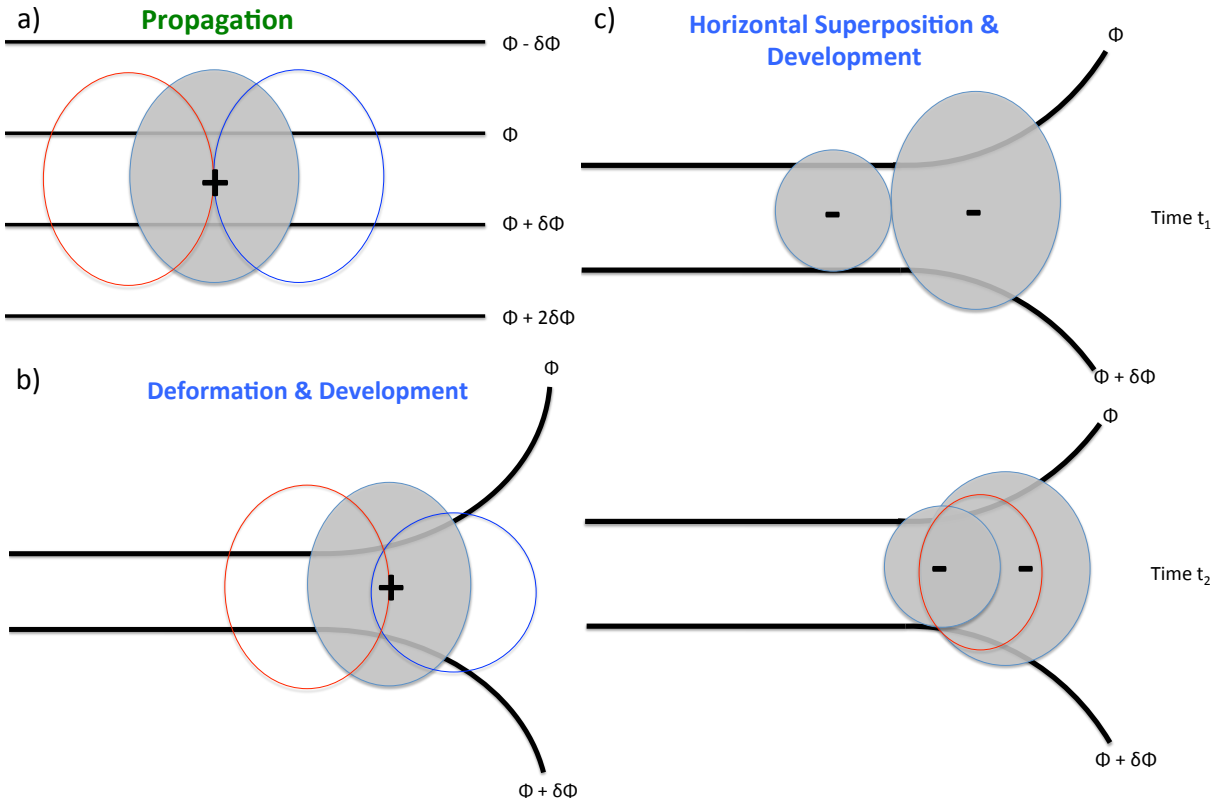

Figure 2. Schematics for processes include in Term A. a) Propagation of a theoretical height anomaly situated within a symmetric, geostrophic background flow, with the location of positive (negative) height tendencies shown in red (blue) open circles. b) Development due to diffluence in the background flow. Note the change in the shape of the height tendencies, indicating development due to the overlap of tendencies and the center of the height anomaly. c) Development due to the horizontal superposition of separate anomalies, differentially advected by the background flow, resulting in overlap at t_2.

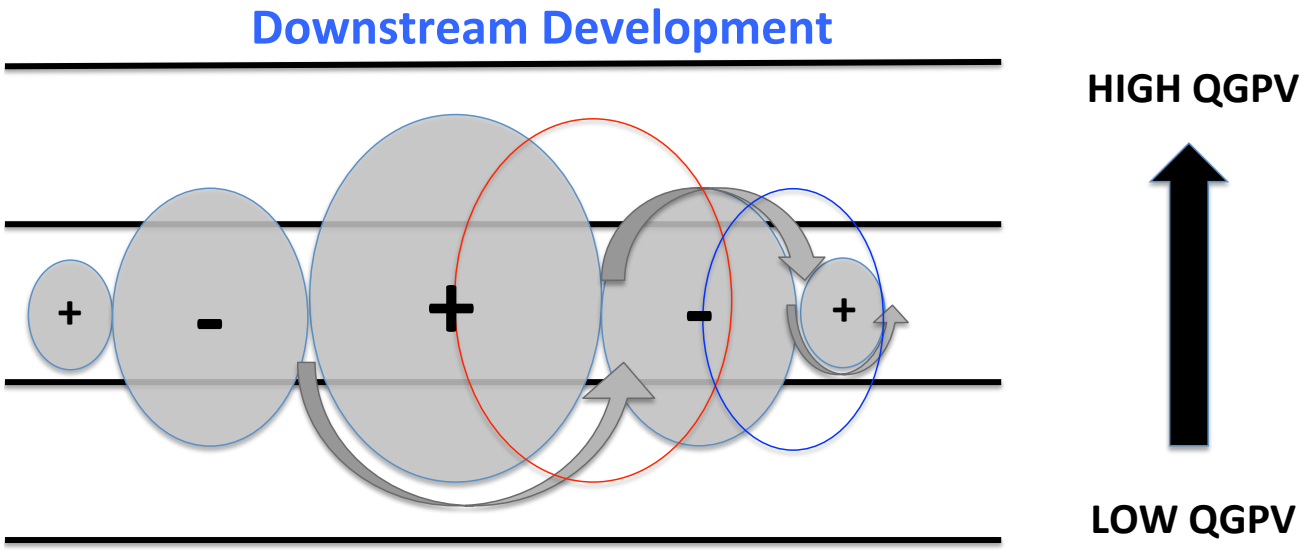

Figure 3) Schematic for Term B, downstream development. Anomalies in a wave packet situated within a background QGPV gradient will advect QGPV, with the influence of the largest anomaly in the center of the packet leading to the growth of the smaller feature downstream. The largest red circle represents height tendencies associated with the largest, center anomaly, cyclonic here, which advects low-QGPV into the center of the smaller anticyclonic feature downstream, leading to height rises and development. See text for explanation.

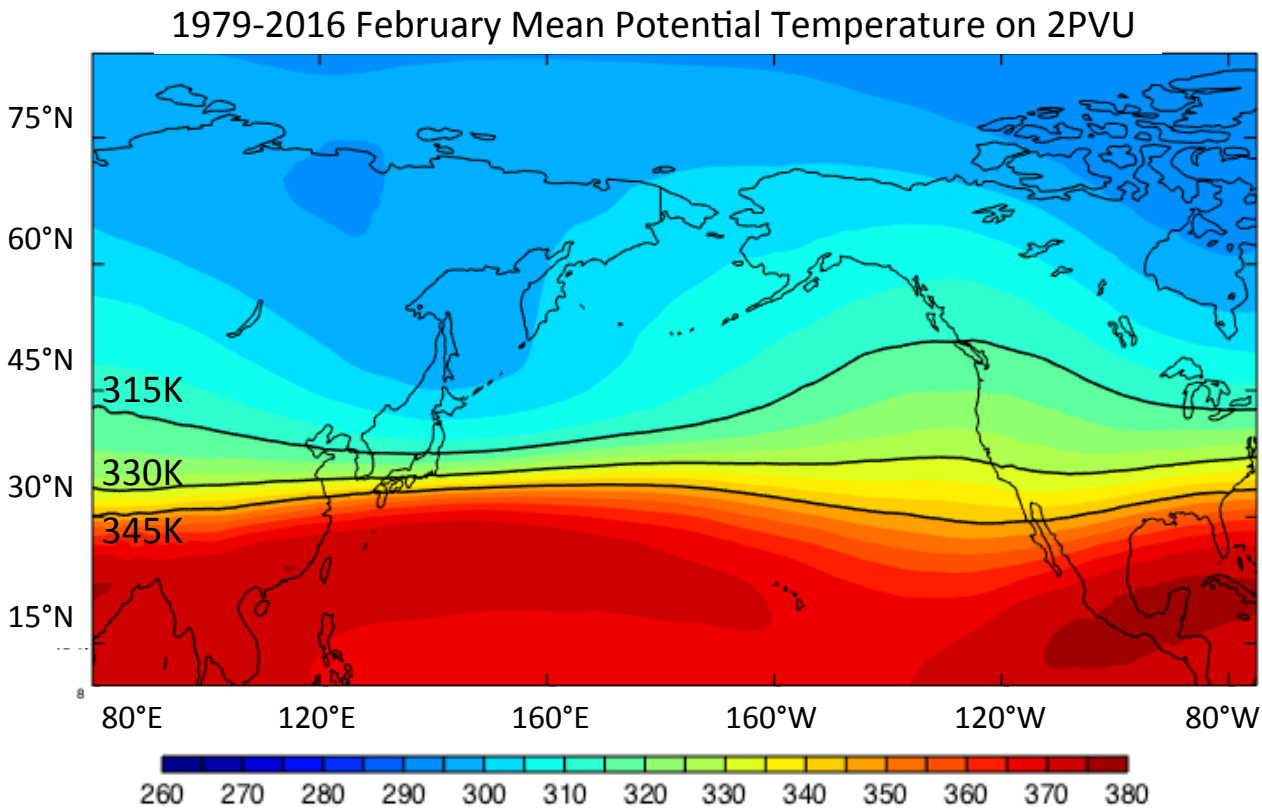

Figure 4: 38-year (1979-2016) February mean potential temperature on 2PVU from ERA-Interim. Fill is potential temperature (θ) in units of K contoured according to the accompanying scale. Solid black contours are the individual 315, 330 and 345 K isentropes.

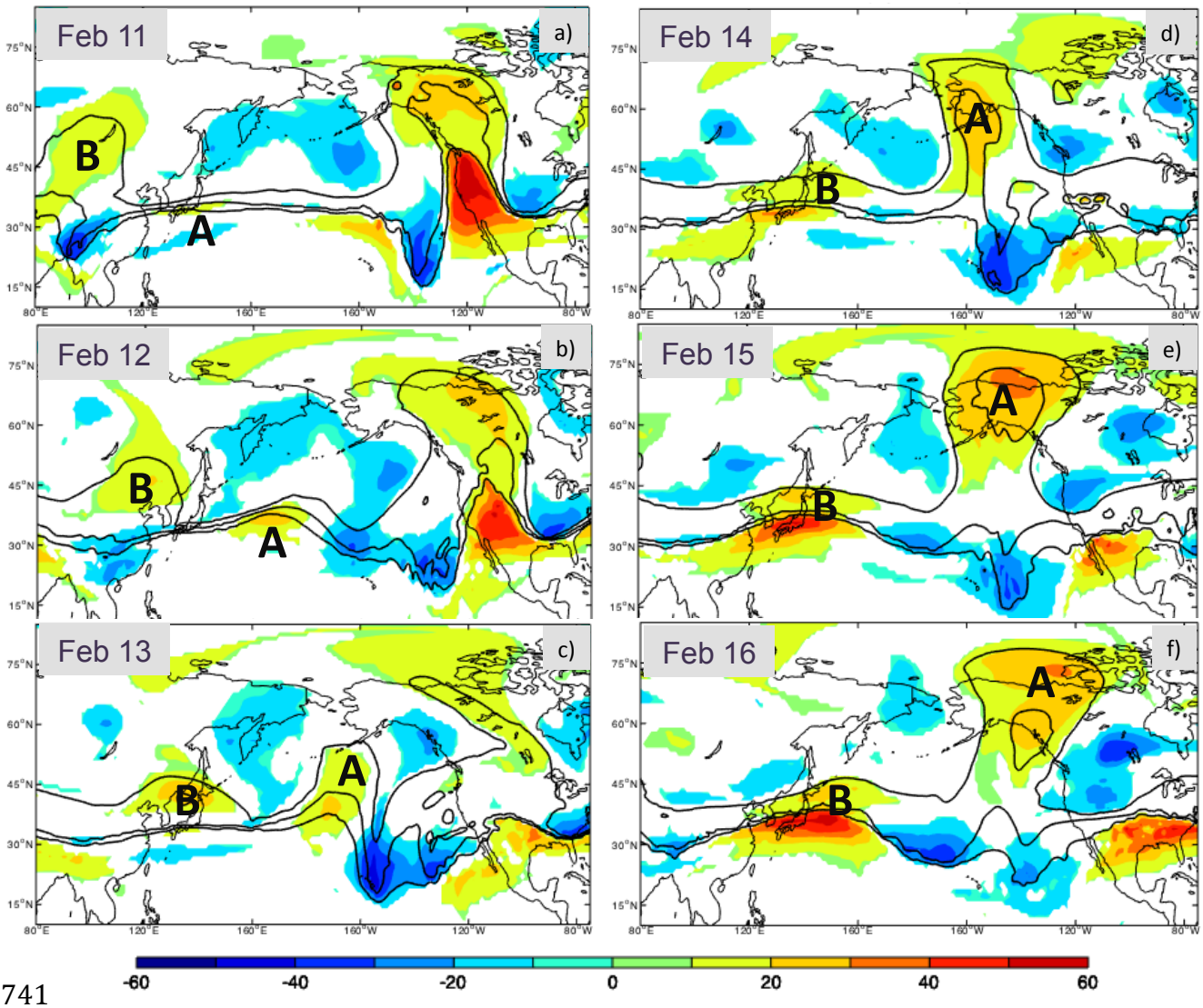

Figure 5: Daily mean potential temperature anomalies (fill patterns in units of K contoured according to accompanying scale) on 2PVU for 11-15 February 2006. Solid black lines are the 315, 330 and 345 K isentropes for (a) 11 February, (b) 12 February, (c) 13 February, (d) 14 February, (e) 15 February and (f) 16 February.

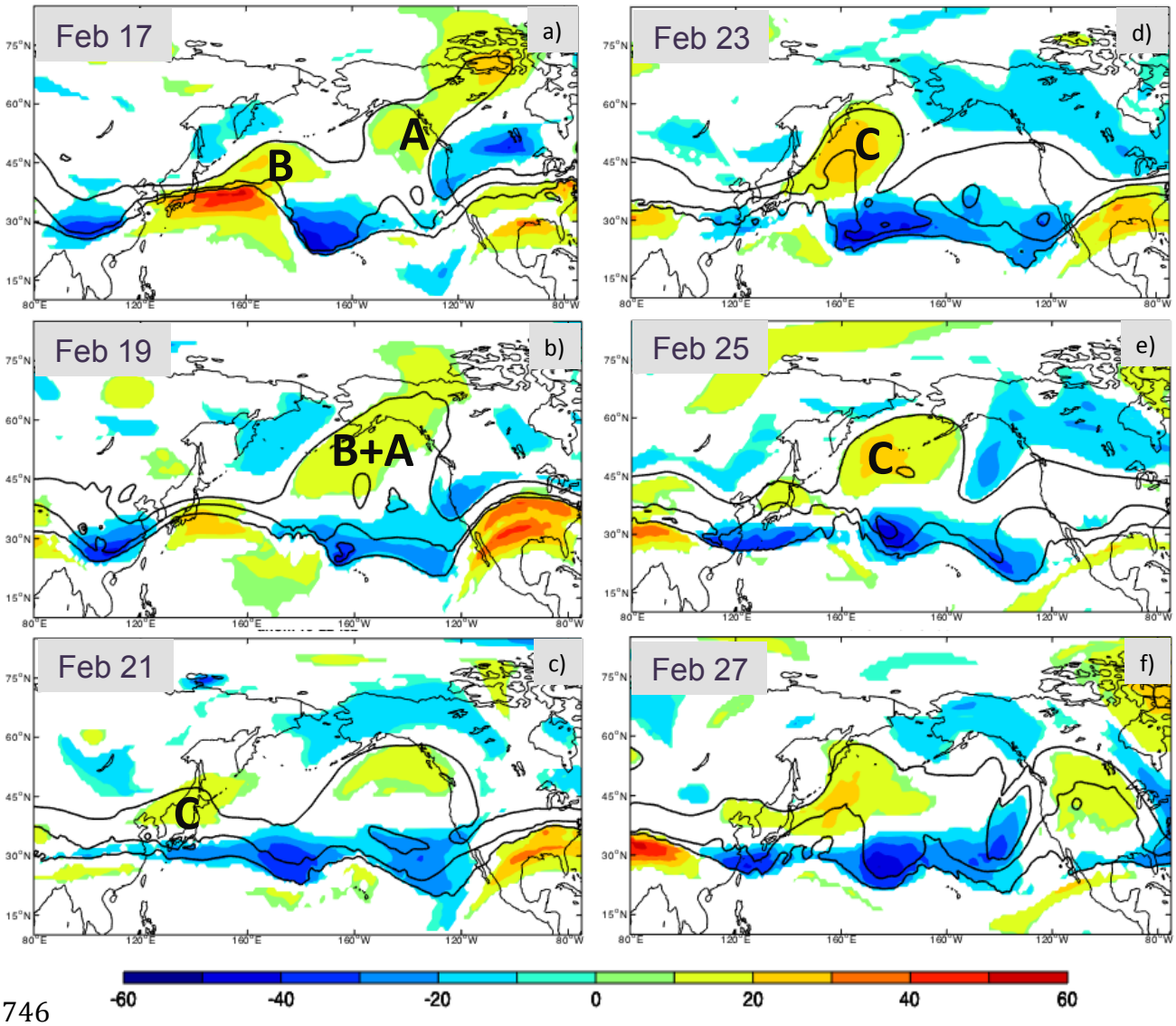

Figure 6: Same as Fig. 5 but for (a) 17 February, (b) 19 February, (c) 21 February, (d) 23 February, (e) 25 February and (f) 27 February.

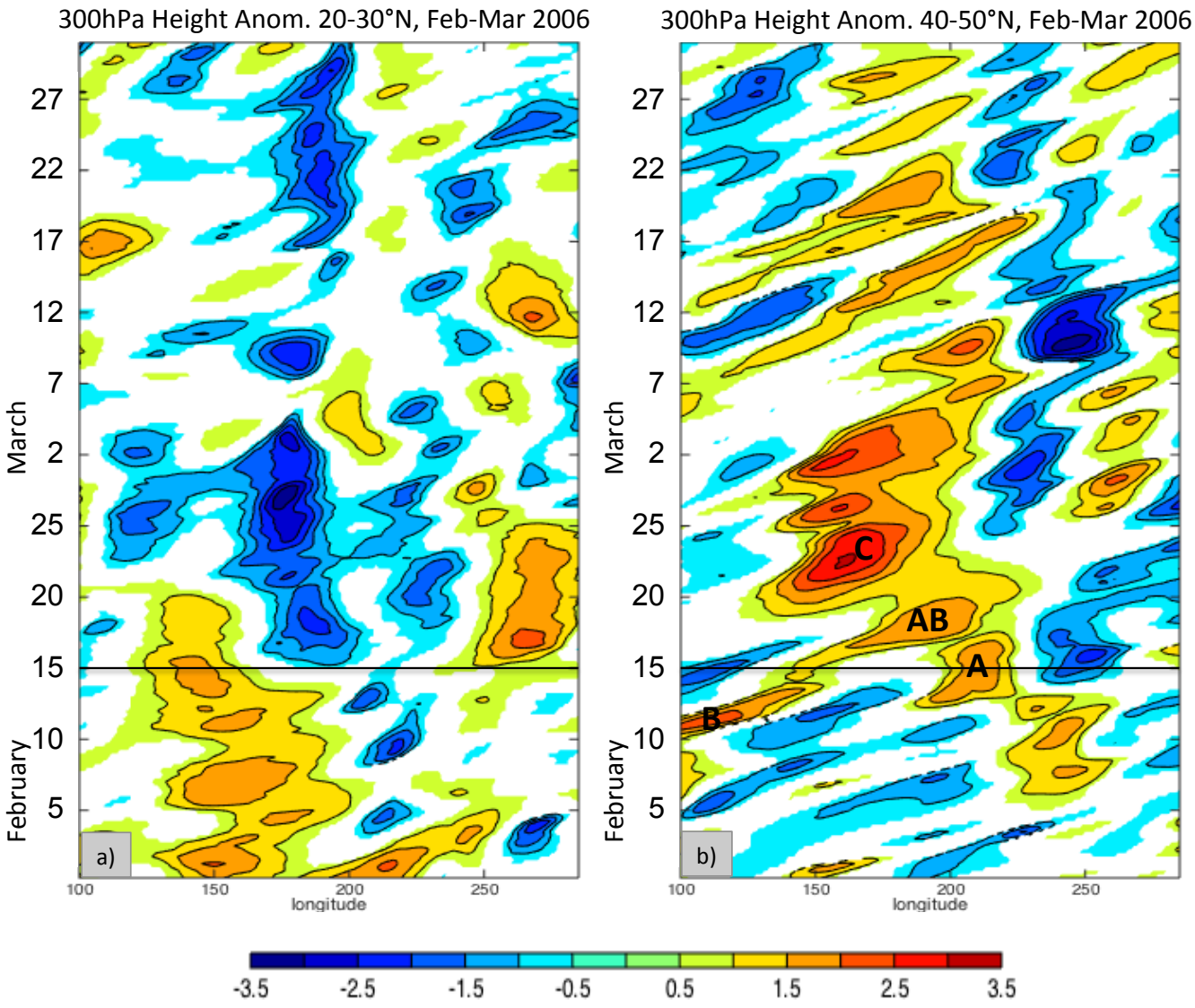

752
753
754 Figure 7. Hovmöller of standardized 300mb height anomalies taken with respect to the 1979-
755 2016 climatology for each day, averaged over a) 20°-30°N and b) 40°-50°N for February-March
756 2006. Black line marks day that retraction is first identified.

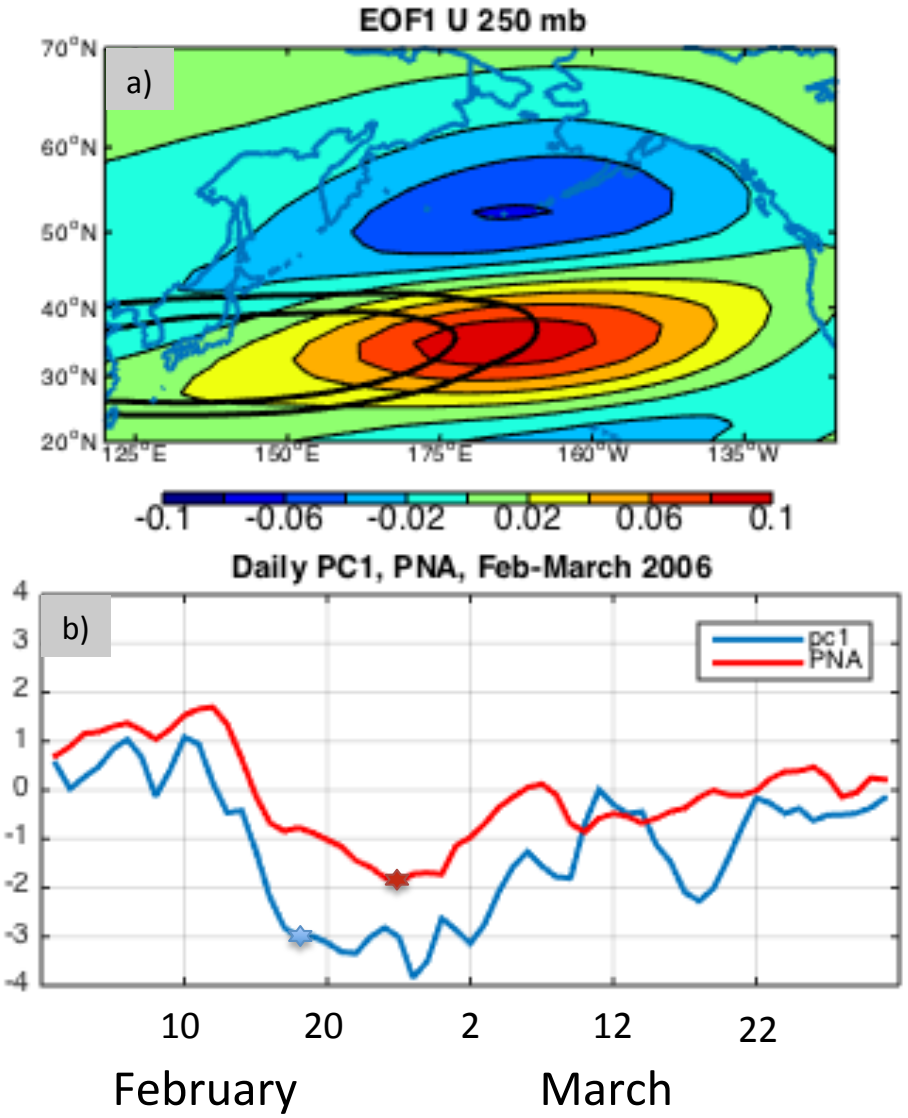

Figure 8: a) Dimensionless EOF1 of 250mb zonal wind shading according to accompanying scale, and 40-50 m s^{-1} December-March 2006 mean 250mb zonal isotachs (solid black lines). b) tandardized daily mean PC1 associated with EOF1 pattern (blue solid line) and the standardized daily-mean PNA index (red solid line). The blue and red stars note when PC1 and PNA are near minimum values, with PC1 leading the PNA.

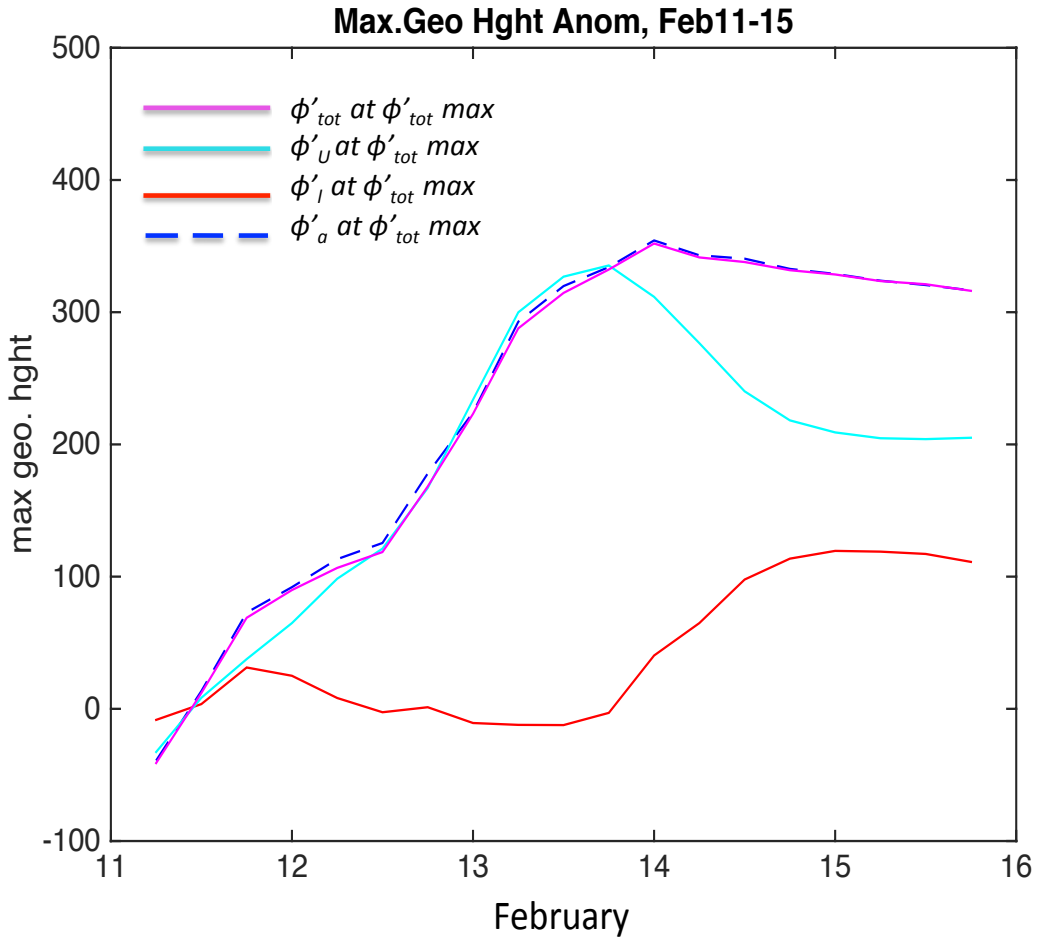

Figure 9: Time series of the maximum 300mb geopotential height anomaly (in magenta) associated with Ridge A using the ERA-Interim (blue) and inverted QG height fields (cyan, red, magenta). See text for explanation.

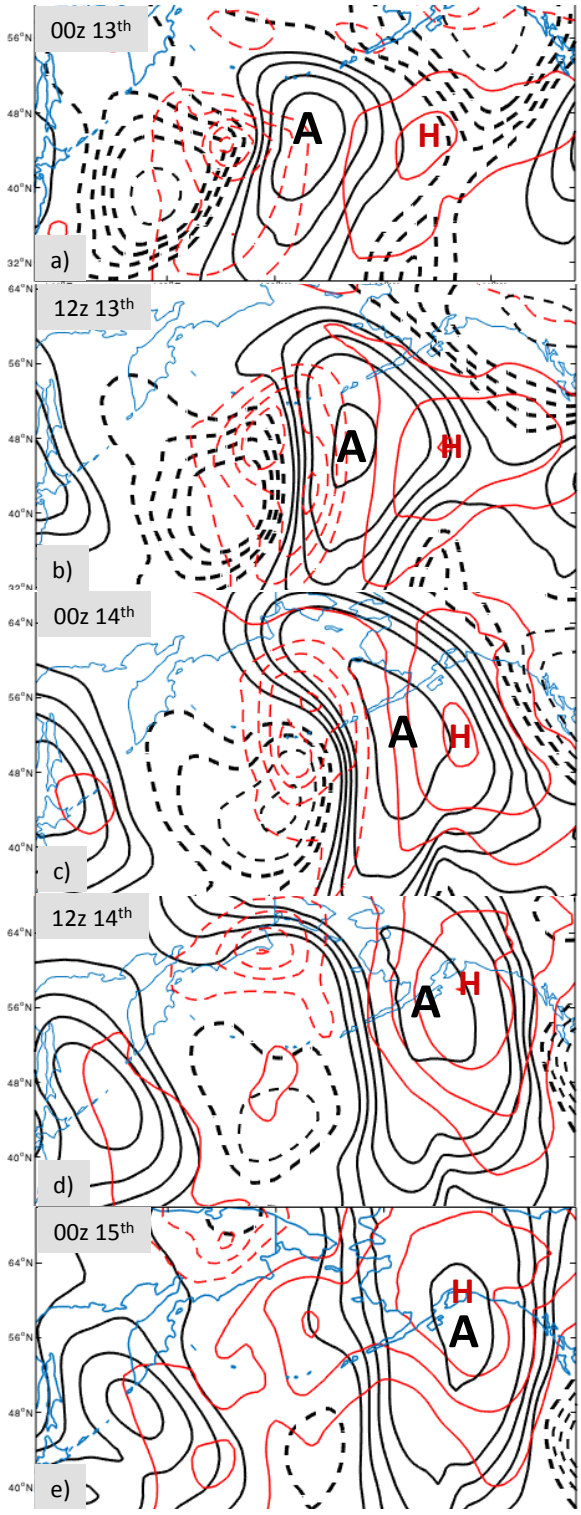

Figure 10: Black (red) contours show 300hPa (950hPa) ϕ_{tot}' from a) 00z 13 February – e) 00z 15 February. Height anomalies are labeled in m and contoured every 50 m with positive (negative) values in solid (dashed) lines. The 'A' denotes the location of Feature A at 300hPa, and the red H marks the location of the 950hPa ridge.

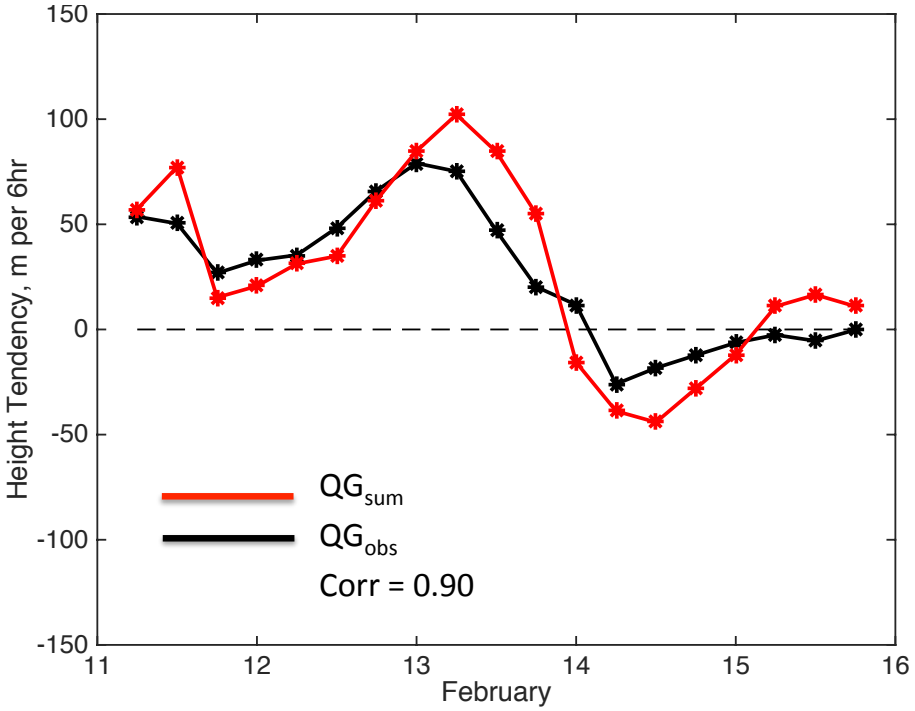

Figure 11: Black line is a timeseries of the 'observed' height tendency of $\boldsymbol{\phi}'_{\boldsymbol{u}}$, calculated using a centered finite difference calculation to produce the QG_{obs} height tendency (Eqn 8) evaluated at the position of the maximum value of the total, inverted QG height anomaly. The red line is the sum of piecewise tendencies (Eqn 6) evaluated at the same grid point. The correlation between the two lines is 0.90. Units for height tendencies is $m*(6hr)^{-1}$.

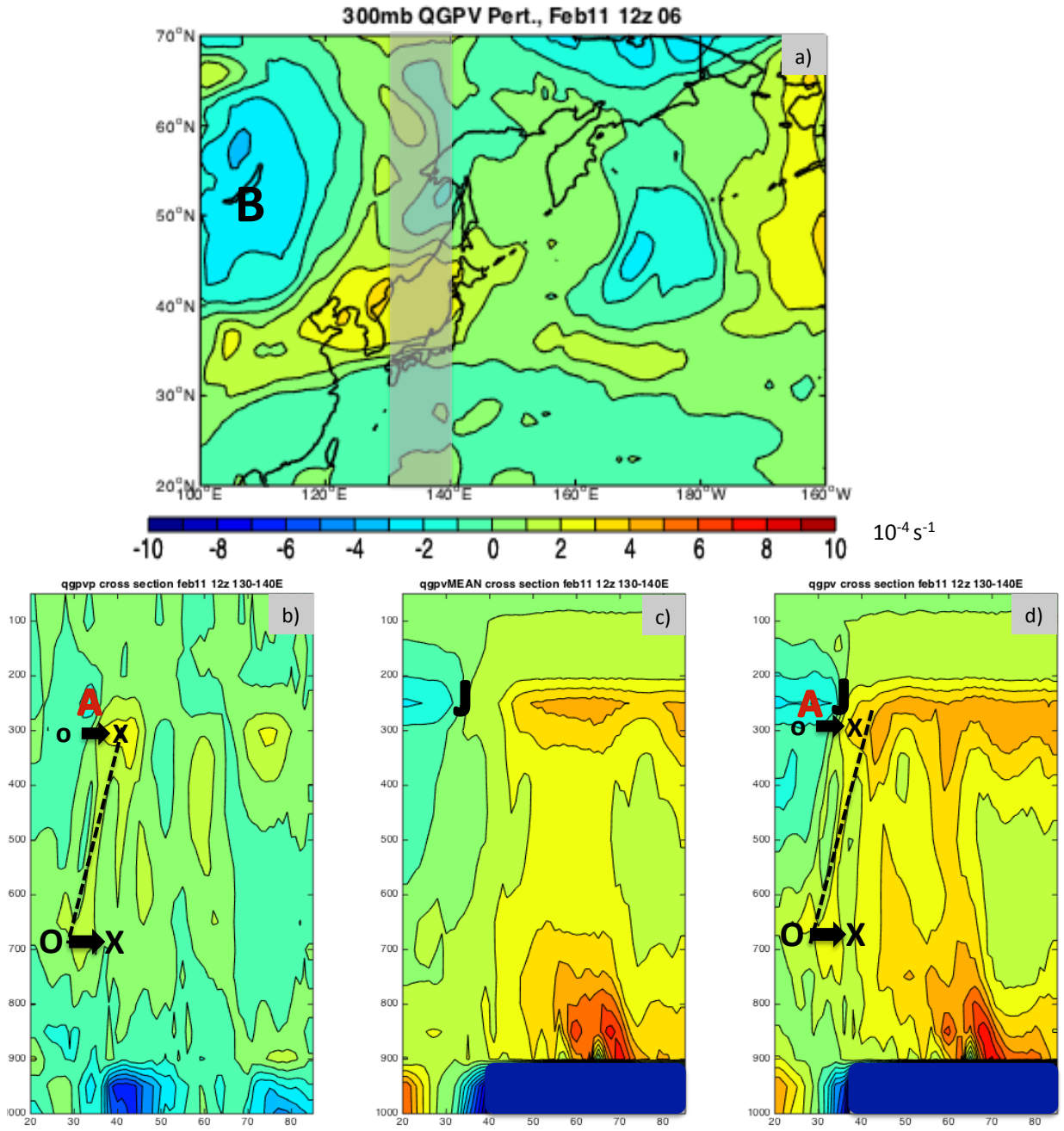

Figure 12: a) Perturbation QGPV at 12z 11 February with location of averaged cross section shown by the light gray box. b)-d) Meridional cross sections, averaged over 130-140°E, of b) perturbation QGPV at 12z 11 February, c) 11-15 February average QGPV and d) total QGPV at 12z 11 February. The respective locations of the jet (J) and Ridge A (A) are indicated. The black dashed lines in b) and d) indicate the axis of the anomalous PV intrusion. The arrows, 'o' and 'x's represent the anomalous southerly flow on the eastern edge of the cyclonic PV intrusion, responsible for the strong negative QGPV advection that results. Units are 10^{-4} s^{-1}.

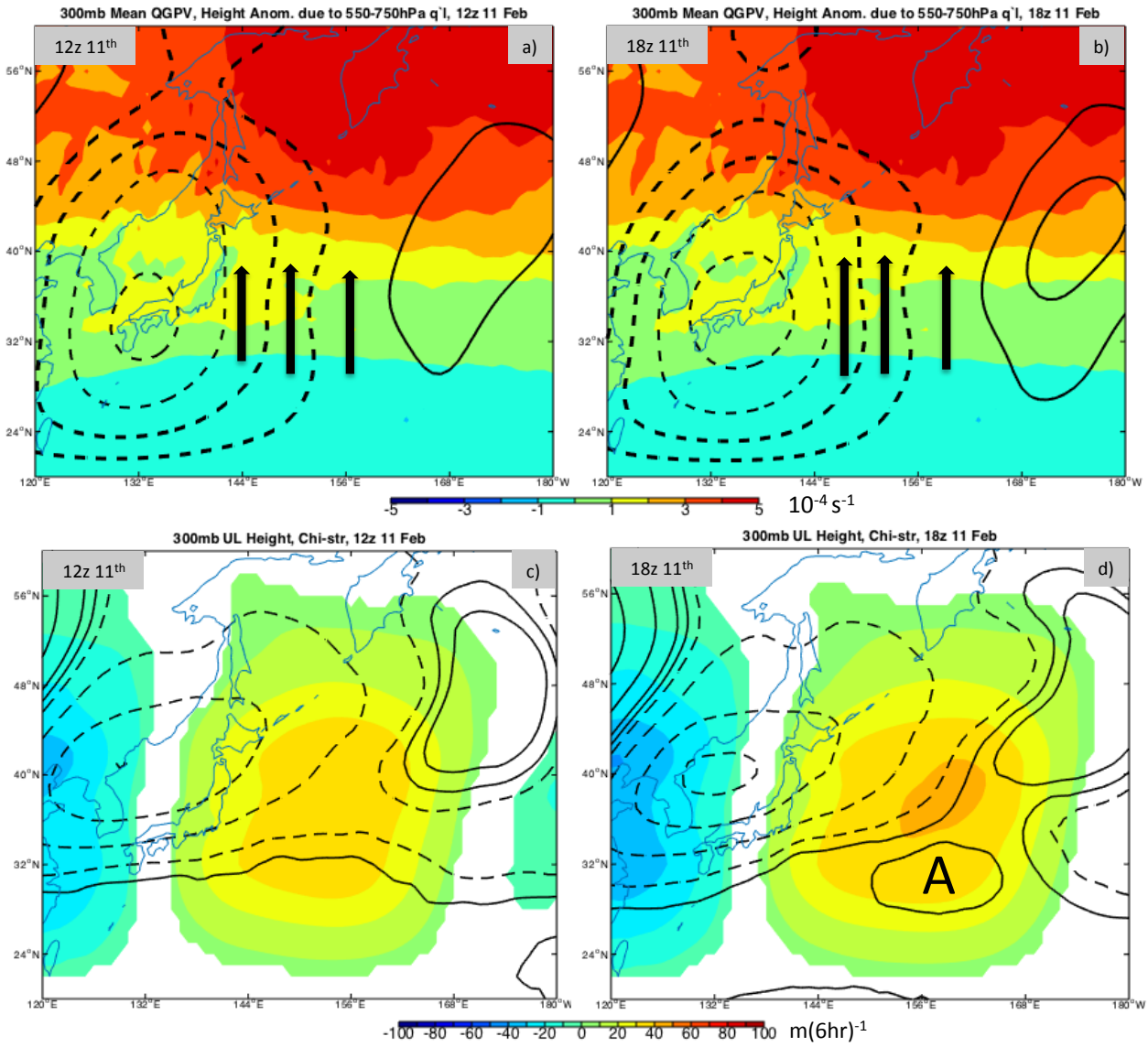

Figure 13:

a) Color shading is the 11-15 February 2006 mean QGPV field at 300hPa labeled in units of 10^{-4} s^{-1}. Contours are the geopotential height anomalies at 12z 11 February associated with 550-750hPa q' in meters, and contoured at 0, +/- 30, 100, 200 300. Solid (dashed) lines indicate positive (negative) height anomalies, and zero is solid. The arrows demonstrate the southerly flow associated with the anomalous circulation from 550-750hPa. Corresponding negative background PV advection and resulting height rises are shown in c). b) As in (a) but for 18z 11 February. c) The color shading is the height tendency pattern resulting from background PV advection by the height field shown in (a). The contours are the 300hPa geopotential height anomalies associated with q_u', contoured as in (a). d) is the same as c) but at 18z 11 February, with Feature A labelled.

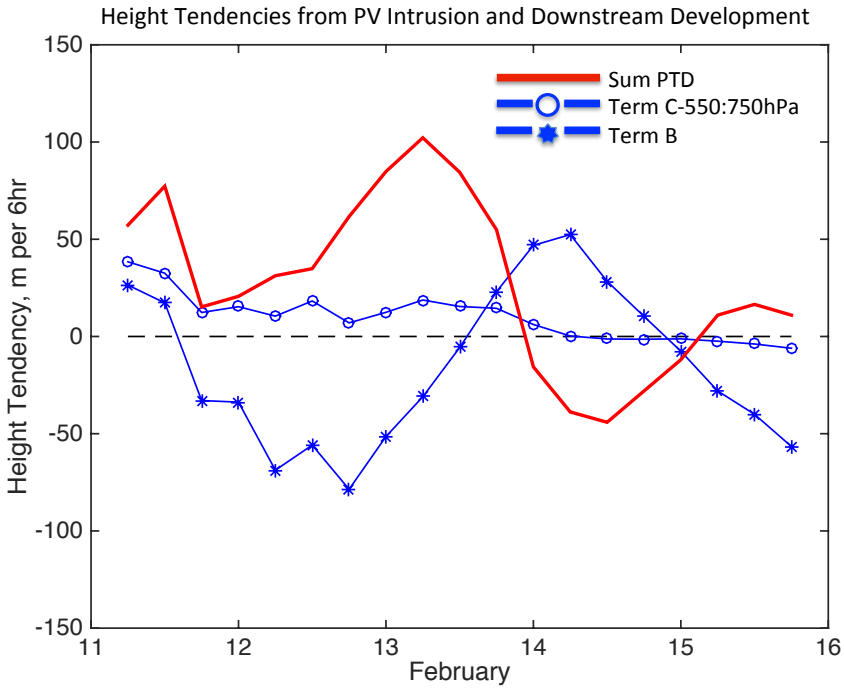

Figure 14: Time series of the height tendencies at the position evaluated in Figures 9 and 11. Term B Eqn (6) (blue stars), Term C (resulting from 550-750hPa only; blue circles) and the sum of all terms in Eqn. (6) (red). Units are meters per six hours.

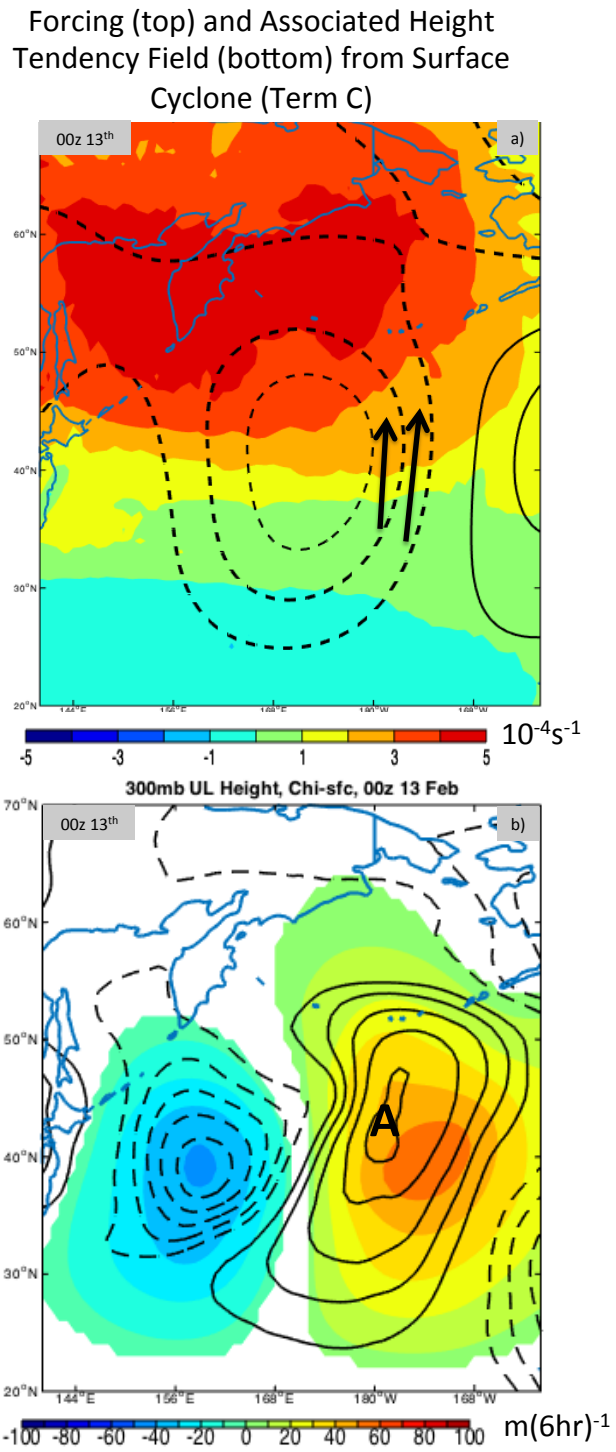

Figure 15: a) As in Figure 13a except the contours are the height anomalies at 300hPa associated with q_l' from 800-1000hPa, ϕ'_{l_intr}, at 00z 13 February. The arrows mark the southerly flow on the surface cyclone's eastern side. b) The color shading is the height tendency pattern attained from inverting $-\mathbf{v}'_{gl} \cdot \nabla\overline{q}_u$, using the geostrophic wind associated with ϕ'_{l_intr}. Contours show the 300 hPa ϕ'_u field, starting at 50 meters at intervals of 50 meters, solid (dashed) lines indicating positive (negative) values.

827

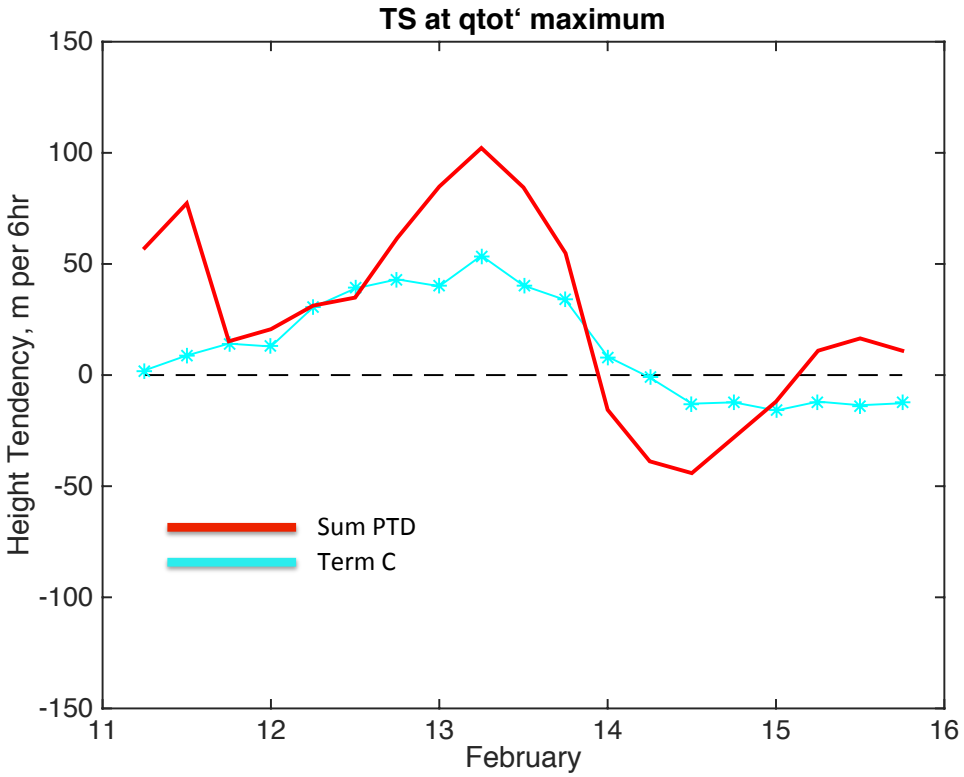

828
829 Figure 16: As in Fig. 14 except for 1000-800hPa component Term C (baroclinic development) in
830 blue.

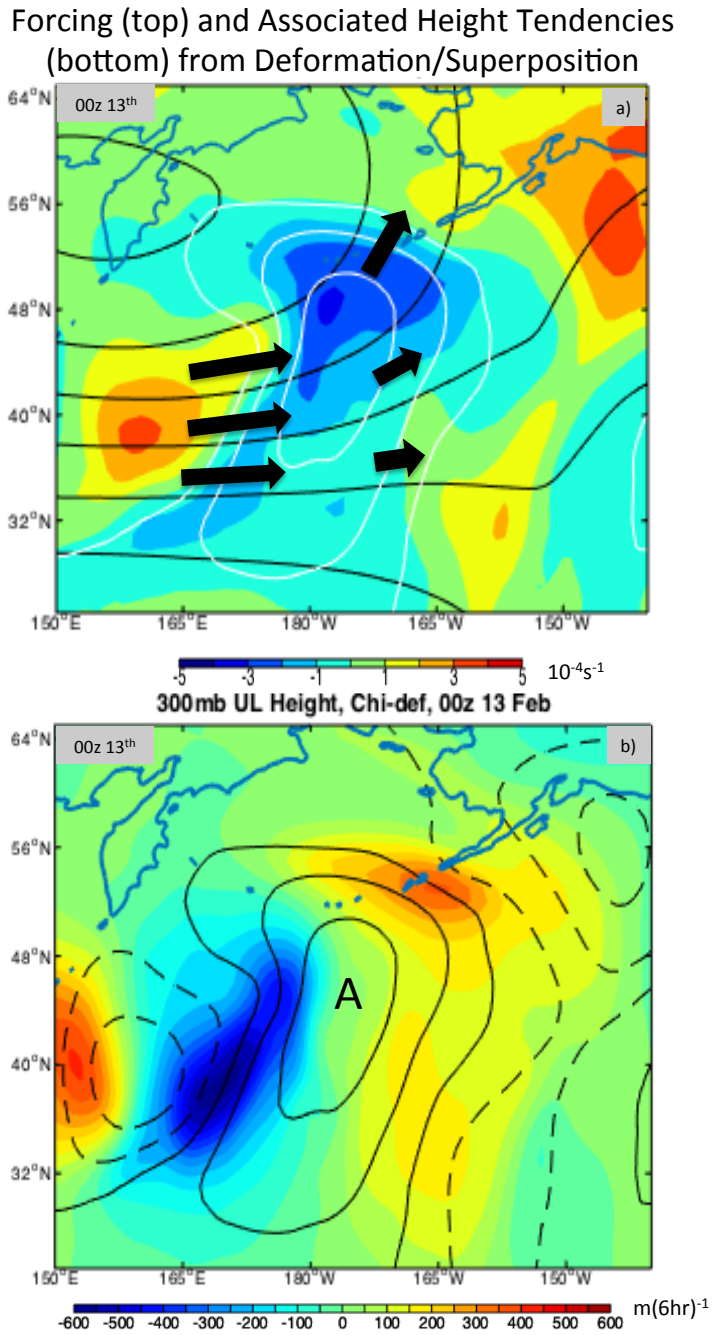

Figure 17: Barotropic Deformation. a) The color shading shows the 300hPa q_u' field, which is being advected by $\overline{\boldsymbol{v}}_g$, parallel to the geopotential height lines (black contours). The arrows indicate the background geostrophic winds and their ability to advect the q_u' field downstream. The white contours show the height anomaly A, and the contour interval is 50m starting at +/- 100 m, positive values only. b) The color shading shows the height tendency field from inverting Term A in Eqn (6), $(-\overline{\mathbf{v}}_g \cdot \nabla q_u')$, at 00z 13 February. Contour interval is 50m starting at +/- 100 m, positive (negative) is solid (dashed) lines, and zero is solid. The A indicates the location of maximum height of Feature A, and positive tendencies overlapping with A indicates that this term is aiding in further development of A.

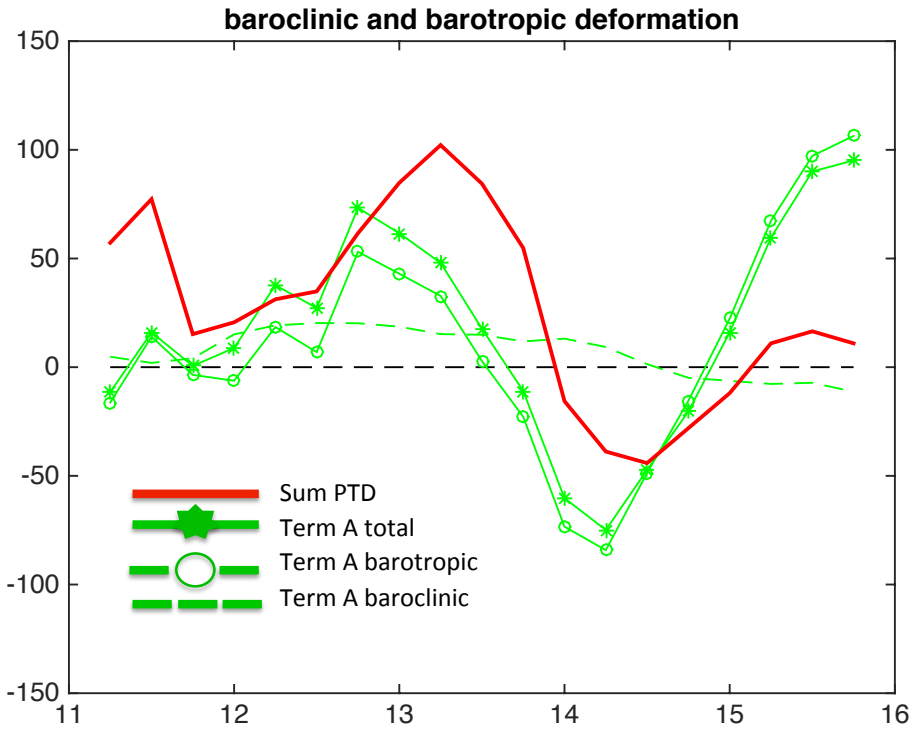

Figure 18: Time series of barotropic and baroclinic contributions to Term A in Eqn (6). The sum of the right-hand-side of Eqn (6) is shown in red. Units $m*(6hr)^{-1}$.

Forcing (top) and Associated Height Tendencies (bottom) from Deformation/Superposition

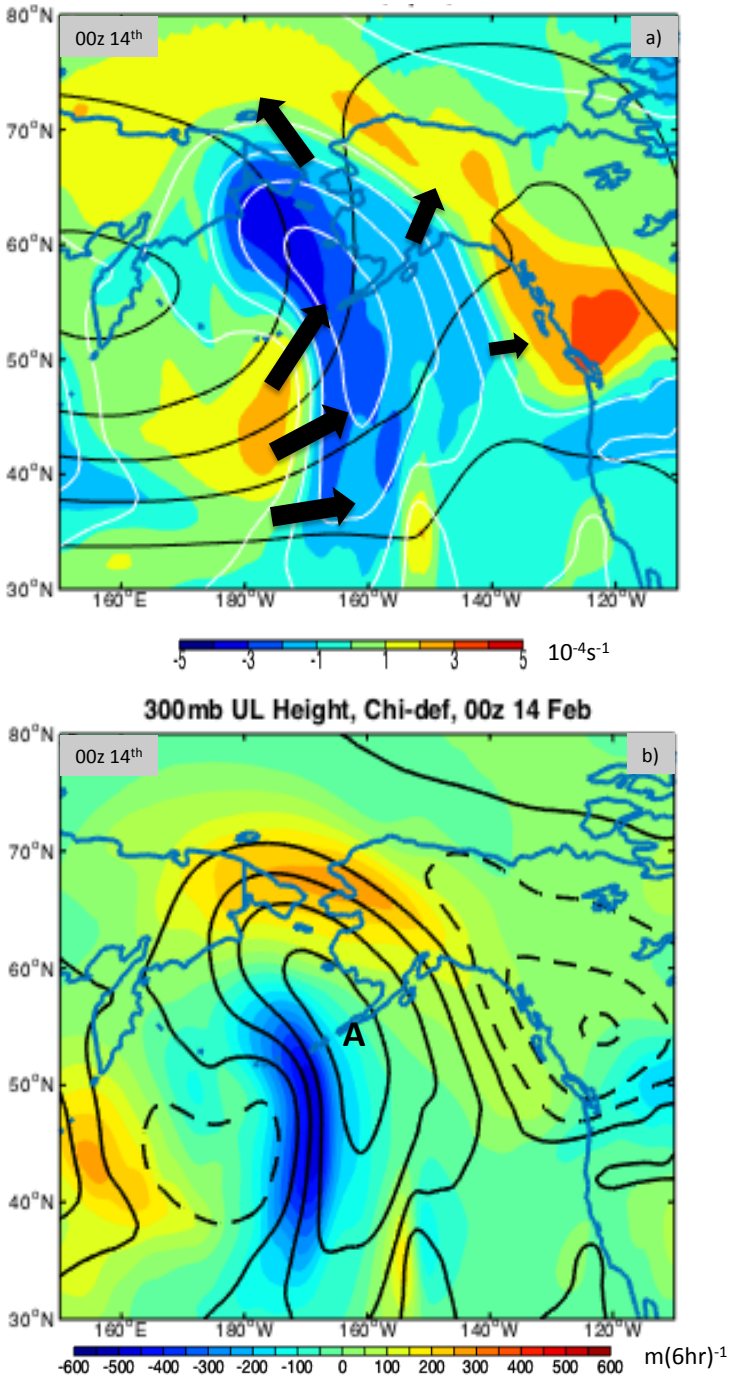

Figure 19: As in Figure 18, but for 00z on February 14th.

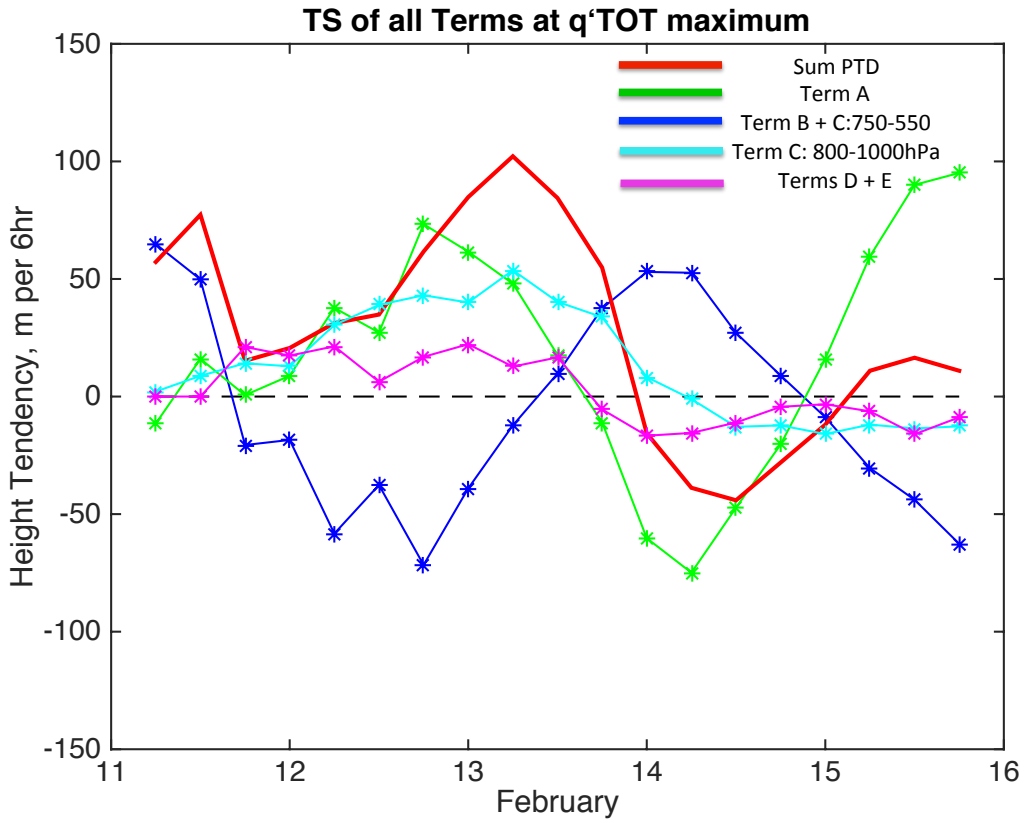

Figure 20: Time series of all terms on the right-hand-side of Eqn (6): Term A, deformation/superposition, is in green, the sum of Term B (downstream development) and PV intrusion component of Term C (baroclinic development, 750-550hPa) is in dark blue, surface component Term C (baroclinic development, 800-1000hPa) is in light blue, and the sum of Terms D and E (vortex-vortex interactions) is in pink. The red line is the sum of all terms in Eqn (6).

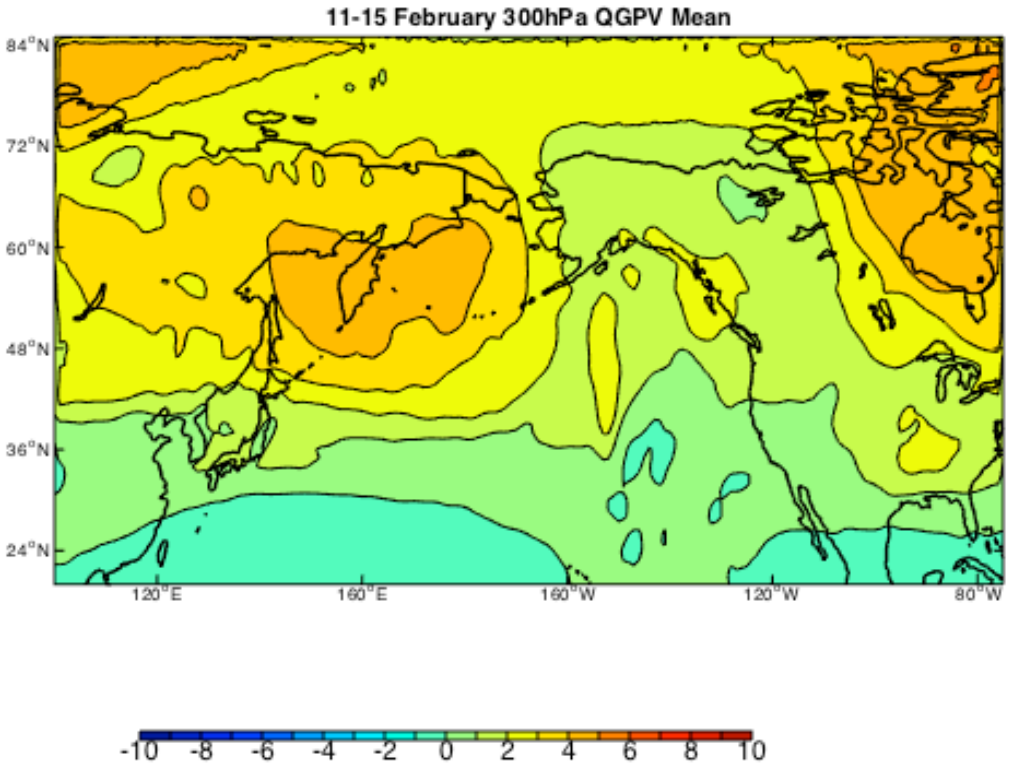

Figure 21: 11-15 February mean QGPV at 300hPa, units 10^{-4} s^{-1}.